Development of an active/barrier bi-functional anti-corrosion system based on the epoxy nanocomposite loaded with highly-coordinated functionalized zirconium-based Nanoporous metal-organic framework (Zr-MOF)

Mohammad Ramezanzadeh, Bahram Ramezanzadeh, Ghasem Bahlakeh, Ali Tati, Mohammad Mahdavian

PII: S1385-8947(20)33485-9
DOI: https://doi.org/10.1016/j.cej.2020.127361
Reference: CEJ 127361

To appear in: *Chemical Engineering Journal*

Received Date: 24 June 2020
Revised Date: 22 August 2020
Accepted Date: 11 October 2020

Please cite this article as: M. Ramezanzadeh, B. Ramezanzadeh, G. Bahlakeh, A. Tati, M. Mahdavian, Development of an active/barrier bi-functional anti-corrosion system based on the epoxy nanocomposite loaded with highly-coordinated functionalized zirconium-based Nanoporous metal-organic framework (Zr-MOF), *Chemical Engineering Journal* (2020), doi: https://doi.org/10.1016/j.cej.2020.127361

Development of an active/barrier bi-functional anti-corrosion system based on the epoxy nanocomposite loaded with highly-coordinated functionalized zirconium-based Nanoporous metal-organic framework (Zr-MOF)

Mohammad Ramezanzadeh[a,*], Bahram Ramezanzadeh[a,**1] Ghasem Bahlakeh[b,***], Ali Tati[c], Mohammad Mahdavian[a]

[a] *Surface Coating and Corrosion Department, Institute for Color Science and Technology, Tehran, Iran.*

[b] *Department of Chemical Engineering, Faculty of Engineering, Golestan University, Aliabad Katoul, Iran.*

[c] *Department of Chemical and Petroleum Engineering, Sharif University of Technology, Tehran, Iran.*

Abstract

For the first time, the Zr-UIO-66 MOF, Zr-UIO-NH_2-MOF, and Zr-NH_2-UIO-MOF particles, covalently functionalized by Glycidyl Methacrylate (GMA@NH_2-UIO), were utilized as the novel functional anti-corrosive fillers. The functionality, high surface area, phase composition, excellent thermal properties as well as chemical stability of the Zr-MOFs were proved by FT-IR, BET, XRD,

[1] *To whom correspondence should be addressed:*
* Mohammad Ramezanzadeh: e-mail: ramezanzadeh-mo@icrc.ac.ir
** Dr. Bahram Ramezanzadeh: e-mail: ramezanzadeh-bh@icrc.ac.ir, ramezanzadeh@aut.ac.ir
*** Dr. Ghasem Bahlakeh: e-mail: gh.bahlakeh@gu.ac.ir

TGA, and water stability tests, respectively. The smart pH-sensitive controlled-release activity of the corrosion inhibitors (i.e., Zr ions and organic compounds) from the prepared Zr-MOFs was proved by the water stability test of the Zr-MOFs particles in the acidic (pH=2), neutral (pH=7.5), and alkaline (pH=12) solutions containing 3.5 wt % sodium chloride. The active inhibition properties of the Zr-MOFs were obtained in saline solution by two methods of (i) the solution phase and (ii) scratched epoxy coated samples containing Zr-MOFs by Tafel polarization method and EIS analysis. According to the EIS data, the excellent barrier (passive) properties of the composite film filled with GMA@NH_2-UIO particles (G-UIN/EP) were proved by the highest impedance level at the lowest *f* (frequency) (log ($|Z|_{10\ mHz}$= 9.86 Ω.cm^2), the lowest value of the breakpoint frequency (log (f_b)= -1.42 Hz) and the highest coating undamaged index (85.93 %) after 120 h of immersion. The salt spray (accelerated corrosion test) test (SST), pull-off (testing the strength of adhesion), and cathodic disbonding test (CDT) experiments showed excellent interfacial-adhesion properties of the G-UIN/EP sample in two dry (unexposed) and wet conditions. The hardness test showed that through the incorporation of the UIO, UIN, and G-UIN particles into the epoxy coating, the hardness, and scratch-resistance of the coating were notably improved.

Keywords: Zr-MOF; UIO; Glycidyl Methacrylate; Epoxy composite; Active/passive corrosion inhibition; MC/DFT/MD modelling

1. Introduction

Carbon steel (CS) is known as the most common types of metals that are widely used in numerous applications [1]. However, the feeble corrosion resistance of CS in the harsh corrosive atmosphere is still a big challenge in different applications in both economic and environmental impacts [2]. There are several techniques to prevent metal from corroding. Organic coatings are commonly known as a good anti-corrosion coating to protect metals from corrosion through barrier shielding

effect against corrosive species [3]. The epoxy resin (solvent-based) is one of the well-known anti-corrosion organic coatings due to the excellent intrinsic anti-corrosion (barrier), appropriate thermo-mechanical properties, and good adhesion bonding to most of the metal substrates [4]. However, the barrier coatings such as neat epoxy lose their barrier role during services due to the degradations, that provide holidays and intrinsic and/or artificial defects within the coatings, causing the penetration of water, $O_{2,}$ and chloride ions as corrosive species to the interface of metal/coating [5]. For many years, the active leachable species such as inhibitive and sacrificial pigments are introduced to overcome this phenomenon [6, 7]. But because of the hazardous nature of some of these conventional anti-corrosive pigments, the usage of many of these materials in the coating formulation has been restricted. On the other hand, the smart controlled release activity of the corrosion inhibitors from some of these fillers is still a big challenge, and long term protection could not be achieved from the coatings incorporated by these fillers. Today, applications of nanomaterials such as nanopigments, nanocontainers, nanofillers become the recent researches topics to enhance the thermo/mechanical and/or active/barrier corrosion protection of the organic coating [8-13]. Through the nanomaterials, the MOFs are considered in the wide range of applications in the past decade [14-17]. MOFs are one of the advanced porous crystalline coordination types of polymers with several extraordinary characteristics [18]. MOFs can be constructed through the donor-acceptor mechanism between the metal clusters (nodes) coordinated by organic ligands (linkers) [19]. This crystalline porous material can be constructed through several methods such as Hydro (solvo) thermal method, electrochemical synthesis, ultrasonic and microwave-assisted methods, mechano-chemical synthesis, and diffusion method [20]. MOFs with a high crystalline subset, high internal surfaces and good thermo-mechanical and chemical stability are conducted in the numerous usages including gas-purification, gas-storage, catalysis, chemical

sensing, and chemical separation to the delivery of drug, ion exchange, magnet, biological applications and light-emitting devices and sensors [21-26]. MOFs, owing to these unique properties and characteristics, is a good candidate for the new area of application in the corrosion and organic coating fields. Fire safety, flame retardancy, and enhancement of the thermo-mechanical properties of the epoxy resins are another new application of the MOFs in recent years [27, 28]. There are just some new reports for the anti-corrosion applications of MOFs in the corrosion fields as a corrosion inhibitor, conversion coating, and thin films to prevent metals from corrosion [29-36]. The high water stability of some kinds of the MOFs such as ZIF-8, UIO, and also the active functionality of the outer surface of them make MOFs as a good candidate to be incorporated into the organic coating for anti-corrosion applications [37-40]. There are just a few published papers regarding the MOFs application in the epoxy-based coatings for barrier (against water) and active corrosion preventative performance enhancement [41-44]. Ramezanzadeh et al. [45] developed a novel graphene oxide nanocarrier decorated by ZIF-8 particles and incorporated them into the epoxy polyamide coating, achieving unique active/barrier anti-corrosion properties. Wang et al. [46] reported MOF-5 decorated with dopamine to upgrade the protection behavior of the waterborne epoxy coatings. Gao et al. [47] constructed the cerium based MOF (Ce-MOF) loaded with benzotriazole with the controlled-release ability for the betterment of the hydrophobicity and corrosion retardation activity. Ren et al. [48] designed metallic anti-corrosion epoxy coating by using zinc gluconate intercalated porous ZIF-8 particles. As observed, MOFs nanomaterial as potent anti-corrosion pigments and nanocarriers for corrosion inhibitors has attracted significant attention. Zirconium-based MOFs (Zr-MOFs) such as UIO-66 are easy lab-scale synthesis MOFs. UIO-66 can be constructed by Zirconium oxide clusters (nodes) coordinated by terepthalic acid (TA) ligands (linkers) in the presence of Dimethylformamide as a

solvent through hydrothermal methods. $Zr_6(\mu_3\text{-}O)_4(\mu_3\text{-}OH)_4(BDC)_6$ metal organic framework (UIO-66) with coordinated $Zr_6(\mu_3\text{-}O)_4(\mu_3\text{-}OH)_4(CO_2)_{12}$ clusters (secondary building units: SBU) was synthesized first in the Oslo University and so named according to this place that was synthesized there (UIO). Charge density of the metal oxide clusters or metal ions, ionic radius and oxidation state are the key parameters in MOFs generation. Due to the high oxidation state of the Zirconium (IV), Zr ions highly tend to O-bonding with the carboxylate groups. In UIO-66, each metal node could be coordinated with up to 12 linker struts. Therodynamice durability of the highly-coordinated Zr-centered MOF (i.e. Zr-UIO-66) is because of the strong Zr-O bonds that formed between the Zirconium and O (Zr-O) atoms in the Zr-MOF structures. UIO-66 has illustrated superior thermal, mechanical, aqueous, water, and moisture stability [49-51]. As it was said, Zr-MOFs is one of the highly stable MOFs that maintains its skeletal structural integrity in the neutral pH, but there are many reports showing that they are not stable enough in the acidic and especially alkaline pHs [52, 53]. This fact becomes important when the local pH on the metal surface immersed in the neutral salty solutions during the electrochemical reaction may become alkaline and acidic as a result of the cathodic ($2H_2O+O_2+4e\rightarrow 4OH^-$) and anodic ($Fe\rightarrow Fe^{2+}+2e$, $Fe^{2+}\rightarrow Fe^{3+}+e$, $Fe^{2+}+2Cl^-\rightarrow FeCl_2$, $Fe^{3+}+3Cl^-\rightarrow FeCl_3$ (acidic salt)) reactions, respectively. The Zr-MOFs can be partially deteriorated in the acidic and alkaline conditions, causing the significant release of the Zr ions and the organic ligands. According to the literature, many cations like Zn, Zr, Ce, and Pr, and also organic compounds (ligands) containing O and N atoms could be adsorbed and/or act as effective corrosion inhibitors on the metal surface and protect the metal surface against corrosion [54-58]. Due to the interesting properties of the Zr-MOFs, it seems that UIO-66 based MOF could be used as filler, anti-corrosion pigment, and corrosion inhibitors nanocontainer in the organic coatings. There are some reports for thermo-mechanical and fire safety applications

of Zr-MOF, such as UIO-66 in the organic coating such as epoxy [59-61]. There are no reports for the anti-corrosion usage/application of the Zirconium-MOFs, i.e., UIO-66, in the organic coating. In this work, the Zirconium-based MOFs *(*Zr-MOFs*)* were constructed by a selection of the terephthalic acid (UIO-66: UIO) and 2-aminoterephthalic acid (NH_2-UIO: UIN) as organic linkers. Glycidyl methacrylate was selected to modify the UIN and bloke the active $–NH_2$ functional groups of the UIN to reach better dispersion within the epoxy coating. Then, the epoxy-based film was reinforced with the UIO, UIN, and glycidyl methacrylate modified UIN particles (GMA@NH_2-UIO: G-UIN) to achieve excellent corrosion retardation potency. The BET, TGA, FT-IR, and XRD testing methods were used to explore the MOFs structural features. The EIS, polarization, cathodic delamination, pull off (adhesion), and SST tests were carried out to MOFs anti-corrosion abilities in the solution and coating phases. As complementary tools, the DFT based ab initio modeling integrated with classical techniques of MC/MD was chosen to basically inspect the affinity, interfacial adsorption, and electronic-structure of Zr-based coordination compounds.

2. Experimental

2.1 Materials

Clear light-yellow Epiran-01 solvent-based epoxy resin (75% solid) and Crayamid (type 115-X70) hardener (50% solid) were purchased from local petrochemical companies, Iran. Ultra-pure Zirconium (IV) chloride ($ZrCl_4$), terephthalic acid, chloroform, tetrahydrofuran (THF), 2-aminoterephthalic acid (2-ATA), DMF and glycidyl methacrylate (GMA) reagents were brought from Merck, and Sigma Aldrich Co. Metal panels (st-12, 12 cm×9 cm×2 cm) as substrates were provided from Mobarakeh steel Co. and cleaned by water and detergent at first. Then, the abraded steel sheets (via emery sandpapers) were degreased by the commercial-grade of acetone solvent.

2.2 Synthesis of MOFs

In our study, the UIO and UIN particles were synthesized with solvothermal process. For the synthesis of UIO, 0.53 g $ZrCl_4$ as a metal source and 0.38 g of TA as a linker was added to 30 ml DMF and stirred magnetically (1000 rpm). The clear $ZrCl_4$/TA containing media was introduced into a 50 ml reactor (Teflon-lined), and for 24 h, at 120 °C, the reaction was continued. Then, the product achieved was settled by the centrifuge process. The white crystalline powders were washed several times with DMF by centrifugation method. Then, the as-synthesized MOF powders were washed 6 times with chloroform by centrifugation (6000 rpm, 10 min) followed by sonication (100-150 W, 2 min) to remove the organic impurity. For further purification, 0.3 g of the synthesized white powder was soaked in about 85 ml chloroform for 6 days. The UIO/chloroform mixture was sonicated (100-150 W, 2 min) and separated by filtration. The obtained product was dried (at 100 °C) during the time of 24 h to achieve the dried UIO product. The UIN particles were prepared by the same procedure, but 0.41 g 2-ATA acid was used instead of TA [62, 63].

2.3 Synthesis of GMA@NH_2-UIO

0.12 g UIN powder was embedded into 10 ml THF and then stirred for half an hour. The UIN/THF mixture was suspended through sonication (100-150 W, 20 min) while the temperature was controlled through the ice-water containing bath. Then, 32 mmol glycidyl methacrylate (GMA) was introduced into the THF solution containing UIN particles and carefully mixed for 30 min. Under mixing (at 55 °C), the reaction was continued for 36 h. Then, the sediment product was settled through 10 min centrifugation (6000 rpm), and the final product was washed by THF four times. Then, the as-synthesized G-UIN powders were washed 4 times with chloroform by centrifugation (6000 rpm, 10 min) followed by sonication (100-150 W, 2 min) to remove the unreacted GMA. The last product was merged into fresh chloroform and magnetically mixed for

24 h and was separated by centrifugation. The washing procedure with fresh chloroform was done sequentially for five times again. The final yellow product was collected and dried at 55 °C under vacuum [64].

Figure 1.

2.4 Water solubility and extract preparation of the MOFs

The water solubility of UIO, UIN, and G-UIN particles was studied in the salty solution through the inclusion of 0.2 g of each MOFs powders into glass vessels containing 100 ml of acidic (pH=2), neutral (pH=7.5), and alkaline (pH=12) solutions containing 3.5 wt % sodium chloride under continuous stirring for 48 h. In the next step, the MOFs containing suspensions were centrifuged for obtaining the extract solution and undissolved particles. The powders were then transferred into an oven (90 °C) for ensuring the drying of the particles during 30 h. The obtained powder was analyzed by XRD to study the phase degradation of the MOFs in the neutral salty solution. The extract solutions were used to measure the Zr ions and the organic compounds in the solution after 48 h. The extracted solutions of MOFs were prepared by the same procedure in the neutral salty solution for the electrochemical study in the solution phase.

2.5 Preparation of MOFs/epoxy composite coatings

The detailed explanations of the MOFs/epoxy composites preparation are presented in the previous work [45]. For this purpose, 0.2 g of UIO, UIN, and G-UIN powders were added to a different vessel containing 28.26 g of epoxy (solvent-based) resin and for 1 h vigorously agitated via a mechanical mixer. An appropriate level of the nanoparticle dispersion in the resin was obtained through sonication for 10 minutes in the ice-water bath. Finally, 21.74 g of hardener (polyamide) was introduced into the neat epoxy and MOFs/epoxy composites and mixed completely. The

prepared epoxy-polyamide composites without and with MOFs particles were diluted by a mixture of solvents (butyl acetate/xylene) to reach acceptable viscosity. Finally, the MS panels were coated by neat epoxy, UIO-66/epoxy, NH_2-UIO/epoxy, and GMA@NH_2-UIO/epoxy composites via coating applicator (BRAIVE, 35200016) with the wet thickness of 120 μm and labeled as EP, UIO/EP, UIN/EP, G-UIN/EP respectively. The coated panels were maintained in the cleanroom with a controlled condition such as temperature/humidity (27 °C and 35%) for 7 days and finally curing for 3 h at 85 °C. For the cured coatings, the thickness was 85 μm.

2.6 Methods and characterizations

X-ray diffraction analysis (XRD, Philips, PW1730, Cu Kα, λ=0.15406 nm), FI-IR (PerkinElmer, 4000-400 cm^{-1}), TGA (Mettler Toledo, 35-900 °C), FE-SEM (Tescan Mira3 LMU), and Brunauere-Emmette-Teller theory (BET, BELSORP-mini II-) were employed to study the structures and phase composition, chemical composition, thermal stability, surface morphologies and the MOFs specific surface area/pore size, respectively. The BET analysis was done under adsorption/desorption of nitrogen at 77 K after 6 h degassing at 150 °C under vacuum. ICP test (ICP-OES, arian Vistaan) and total organic carbon (TOC) analyzer (SHIMADUZ, TOC-L) were used to measure Zr ions and organic compound concentration in the extract solutions, respectively. In this study, the electrochemical studies were applied in the saline media. Polarization and EIS tests were done on the prepared steel specimens (with an exposed dimension of 1cm×1cm) subjected to the solutions with the MOFs extracts. The protection (active/barrier) behavior of the EP, UIO/EP, UIN/EP, and G-UIN/EP samples was investigated on the intact (2 cm×2 cm) and scratched (1 cm length, and 2 cm × 2 cm exposed dimension) samples by EIS. The electrochemical measurements were done according to the device settings reported in the literature using Ivium Compactstat electrochemical instrument (B09031, Netherlands) in the adjusted frequencies

between 10000 Hz to 0.01 Hz and fixed amplitude equal to ±0.01V. The Tafel test was done in a potentiodynamic mode with a defined scan-rate of 0.01 $V.s^{-1}$ between -200 to +200 mV [45]. The adhesion strengths were investigated in both dry (unexposed) and wet (exposed) conditions by the pull-off method, CDT, and SST. In the CDT, constant -2.0 V potential (vs. SCE) was applied on the samples (with EP) with a 5 mm hole produced in the center, and 3 cm × 3 cm exposed area after immersion in the salty (3 wt % NaCl) electrolyte. The cathodic disbonding radius was measured by digital calipers, and digital images were prepared. SST was conducted on the scratched samples exposed to the SST condition (SHT-214D, Radian Sanat, Iran), followed by the ASTM B117 test method. FE-SEM test method and EDS-map analysis were conducted to study the corrosion product morphology/composition. The Pull off (DeFelsko, PosiTest ATA model) experiment was applied to the samples (after 14 days SST test and before exposure). The Zsimp and Ivium software were employed to analyze the EIS data. Finally, the hardness of the EP, UIO/EP, UIN/EP, and G-UIO/EP samples were measured by Vickers Micro Hardness (Koopa, Model: MH3, Iran), Pendulum (Konig) Hardness (Sheen Instruments LTD, U.K.), and the scratch (Elcometer, 100 W, 230 VAC, 50/60 Hz, E.U.) tests. For the Vickers micro-hardness, the stylus applied a constant force of 0.1 kg at an indentation time of 10 seconds on the surface of the coatings and the morphology of the Vickers indent, Vickers hardness (MPa) value, and diagonal lengths (mm) were reported. For the Konig hardness test, the time (second) taken for the amplitude to decrease from 6° to 3° (ASTM D4366-16) is a good parameter to determine the surface hardness of hard organic coatings. For the scratch test, the weighted stylus tool moves slowly on the surface of the coating under variable applied loadings (kg), and the value of loading that caused the tool contact with the metal substrate was detected as the coating's resistance to the penetration and scratch.

2.7 Modeling approach

2.7.1 Geometry equilibration

The geometries of zirconium (IV)/organic linker complexes were submitted to microscopic equilibration, which was fulfilled with DFT-based modeling embedded in the code of DMol^3 [65]. The complexes of zirconium (IV) or Zr^{+4} with terephthalic acid (TA), and its modified forms, namely 2-aminoterephthalic acid (ATA) as well as GMA-functionalized ATA (denoted as GMA-ATA) were built with bonding 2-6 ligands to tetravalent Zr^{+4} species. The ligands bonding to Zr^{+4} was executed via oxygen (i.e., carbonyl type) atom of bare/modified terephthalic acid. The resulting complexes are $[Zr(TA)_n]^{+4}$ (related to terephthalic acid), $[Zr(ATA)_n]^{+4}$ (related to 2-amino-terephthalic acid), and $[Zr(GMA\text{-}ATA)_n]^{+4}$ (representing the GMA-bonded to ATA molecule). The geometries graphically displaying the Zr^{+4} based complexes are illustrated in **Figures 2** and **3** and the **Supplementary Information Figure S1**. The aqueous medium (given by COSMO model [66]) equilibration of complexes geometries was attained utilizing GGA/PBE scheme in combination with the DNP function. For the attained zirconium (IV) compounds, useful electronic structure factors were elucidated: orbitals (namely HOMO/LUMO) graphics and eigenvalues (that is E_{LUMO}/E_{HOMO}), related eigenvalue gap (designated by $\Delta E_{L\text{-}H}$), and the electrons shared (expressed as ΔN). The computation of the last parameter necessitates the evaluation of other descriptors given previously [67, 68].

Figure 2

Figure 3

2.7.2 Adsorption modeling

The absorptivity of the aforementioned complexes above the target substrate (i.e., steel explained by Fe(110) [67, 69, 70]) was theoretically modeled in the gas phase (using MC method) and also in the aqueous environment (through dynamic approach depending on MD). The adsorption modelings were progressed with extensively chosen FF (force field) of COMPASS [65, 69]. For both modelings, the complexes equilibrium structures along with point charges extracted from DFT were employed. The aqueous environment chosen for MD was explicitly created by making use of the extra layer placed over the metallic layer. This extra layer encompassed solvent molecules and ionic materials (cation of sodium and chloride anion). Before the usage of MD, the prepared complexes cells were optimized with minimization of energy, which lasted approximately 50000 steps. Following this step, MD modeling continued for 1 ns was fulfilled in an ensemble of NVT. The NVT time step and its temperature were equal to 1 fs and room temperature, respectively. Additionally, the atoms of the metallic layer were fixed at bulk positions within atomistic modelings and cell optimization

3. Results and discussion

3.1 MOFs chemical/microstructure investigation

3.1.1 Detailed level FT-IR analysis

FT-IR illustrated the chemical composition of the Zr-MOFs, and results were collected in **Figure 4-a.** For UIO, the weak board absorption band at 3400 cm^{-1} and the respective bands appeared in the wavenumbers of 2850-3100 cm^{-1} indicate the intercrystallite absorbed water and C-H vibration (stretching mode) in the aromatic and/or aliphatic state of the benzene ring and probably DMF, respectively. The symmetrical and asymmetrical stretching vibration modes of the carboxylate groups were demonstrated by intense modes in the range of about 1710-1200 cm^{-1} [71]. The

characteristic peaks centered at about 1655 cm^{-1} and 1586 cm^{-1} reveals the carbonyl (in stretching vibration mode) vibration that is ascribed to the metal clusters (Zr) coordination with the organic ligand and C-O-C bond stretching (in the asymmetric form) of in the terephthalic acid ligand, respectively. At about 1507 cm^{-1} and 1403 $cm^{-1,}$ two peaks are observed that are ascribed to the benzene ring's typical frame vibration [72-75]. There is an un-intense peak at about 1706 cm^{-1} that could be related to the unreacted COOH groups' presence on the MOF particles surface and/or the unreacted ligands [76]. Due to the merging of the vibrational bending of C-H and –OH with Zr-O at lower frequencies (that are presented at about 808, 745, 660, 526, and 483 cm^{-1}), it is not completely clear to demonstrate them [77]. The peaks at about 483 cm^{-1}, 526 cm^{-1}, and 660 cm^{-1} indicate the vibrations of μ_3-OH bond, Zr-O bond, and the stretching (asymmetric) of μ_3-O bonds, respectively [73, 75, 78-81]. The peaks that appeared at about 745 cm^{-1} correspond to the C-H absorption band [82]. Like the UIO, 1400-1700 cm^{-1} wavenumbers reveal different stretching modes of COOH groups [64]. Also, results evidenced two peaks positioned at 1573 cm^{-1} (C=C) and 1654 cm^{-1} (carbonyl). The presence of the primary $–NH_2$ group in UIN was proved by the absorption peaks positioned at 3456 $cm^{-1,}$ and 3366 cm^{-1}, indicating the asymmetric-NH_2 and symmetric-NH_2 vibrations, respectively [83, 84]. The intensity of the second amine bond decreased due to the overlapping of the second N-H bond with the –OH absorption mode. The weak peak at about 1624 cm^{-1} and the peaks observed at about 1386 cm^{-1} are connected to the N-H (in bending mode) and stretching of C-O, respectively [85]. The C-N bonding of the aromatic carbon and N atom (C-N) in the ligands are presented at about 1258 cm^{-1} and 1338 cm^{-1} [83]. The bands observed in 2850-2950 cm^{-1} range in the UIN correspond to C–H bond vibration of the unsaturated and saturated carbons [86]. For G-UIN, one sharp and one depressed absorption peaks related to the $–NH_2$ can be observed. The peak occurred at about 1732 cm^{-1} reflects the ester C=O

bond vibration in GMA attached to the UIN [64]. The FT-IR data showed good agreement with the literatures.

3.1.2 XRD analysis

The UIO, UIN, and G-UIN particles XRD patterns with the characteristic peaks of the MOFs and corresponded reflection planes are shown in detail in **Figure 4-b**. A good degree of the MOFs crystallinity was proved by the sharp/intense peaks observations in the XRD pattern. The more important diffraction peaks with higher intensities placed at 2θs=7.5°, 8.7°, and 25.8°, that are ascribed to the (111), (002) and (006) reflection planes, respectively, were used to estimate the MOFs particles crystallite size. The measured crystallite sizes (by Scherer equation) of the UIO, UIN, and G-UIN are equal to 192.3, 246, and 215.33 nm, respectively. The results are similar to the previous reports [81, 83, 87-89].

3.1.3 TGA analysis

The thermal stability of UIO, UIN, and G-UIN particles was studied by TGA, and derivative TG (DTG) **(Figure 4-c)**. TGA test outcomes evidenced the more thermally stability of the UIO-66 than UIN and G-UIN particles in the almost all range of the temperature. For UIO, there are three separate stages of weight loss in the TGA diagram at about below 100 °C, between 150-350 °C and 450-600 °C which are ascribed to the water evaporation, detachment of the trapped solvent such as DMF and/or hydrolysis of organic ligands and finally break-down of the coordinated nodes bonded to the organic ligands, respectively [75, 89]. Three characteristic steps of weight loss were observed at around 100 °C, between 200-250 °C and between 350-600 °C, evidencing the adsorbed water loss, the removal of the trapped solvents (DMF) from the pores (and/or dehydroxylating of

the Zr oxoclusters) and degradation of the coordinating center of NH_2-UIO and MOF decomposition to CO_2, ZrO_2 and CO, respectively [25, 90, 91]. With comparison to UIN, it seems that the dehydroxylating and decomposition of GMA@NH_2-UIO happens faster. DTG diagram shows a board peak for G-UIN. It could reflect the low stability of the GMA molecules grafted to the primary –NH_2 groups of UIN against high temperature and hydrolysis of the functional groups of GMA. In higher temperatures, the value of residue, the ash of G-UIN, is more than the UIN that could be related to the GMA.

3.1.4 BET analysis

The N_2 related isotherms of the MOFs **(Figure 4-d)** were considered. The value of BET, the specific surface area of the UIO, UIN, and G-UIN particles are 823, 576, and 568 $m^2\ g^{-1}$, respectively. This is a confirmation of the previously reported data [92]. Other data, such as total pore volumes ($cm^3\ g^{-1}$), and the mean diameter (nm) of the MOF particles pore, are collected in **Table S1**. Due to the presence of mesopores (in range of 2-50 nm) in the MOFs, the hysteresis loop was observed in the N_2 isotherms in the relative pressure (introduced by P/P_0) between 0.8-1.0. Lower $a_{s,\ BET}$ and pore volume of G-UIN compared to UIN is due to partially pores blocking of the UIN particles by GMA.

Figure 4

3.1.5 Morphology of MOFs

The MOFs were examined by FE-SEM, as depicted in **Figure 5**. The obtained images revealed round-shaped crystals morphology of UIO particles with average sizes ranging between 80-180

nm. The triangular base pyramid-shaped (with symmetrical crystalline) morphologies with the average sizes between 80-280 nm were observed for UIN and G-UIN. These observations are similar to the morphology reported in the literature [93].

Figure 5

3.1.6 Water stability study of the MOFs

The water stability and Zr ions and organic compounds release properties of the MOFs in the saline solutions were studied by the procedure that was mentioned before. The XRD, FE-SEM, and ICP-OES and TOC analyses were conducted for the Zr ions and organic compound release ability (as a result of the phase degradation) investigation. The XRD results and FE-SEM images of the dried UIO, UIN, and G-UIN particles after 48 h exposure to the neutral (pH=7.5) chloride solution are displayed in **Figures S2** and **S3,** respectively. The XRD patterns showed no significant changes in the crystallinity. No significant changes were observed in the peaks with higher intensity placed at about 2θs≈7°, 8° and 25° that is corresponded to the (111), (002) and (006) reflection planes of the MOFs, evidencing the high stability of the MOFs structure in the neutral condition. The morphological stability of the MOFs was also studied by FE-SEM images. The round-shaped shape of UIO particles and the triangular pyramid-shaped of the UIN and G-UIN particles were not changed after 48 h exposure. The concentration of the Zr ions and organic compounds released in the extracted solutions are provided in **Table** 1, and the results evidenced more Zr ions (Zr=4 ppm) and organic compounds (TOC=8 ppm) concentrations in the extracted solution of UIO compared with the UIN (Zr=3 ppm, TOC=7 ppm) and G-UIN (Zr=2 ppm, TOC=5 ppm) samples in the neutral condition (pH=7.5). The lowest amount of Zr and organic compounds in the extracted solution (pH=7.5) belonged to the G-UIN, indicating the controlled dissolubility behavior of the modified UIN in the neutral pH. The release study of the UIO, UIN, and G-UIN particles in the

acidic (pH=2) and alkaline (pH=12) salty solutions after 48 h, showed the high Zr ions and organic compounds concentration in the solution, indicating the more phase degradation of Zr-MOFs in the acidic and especially alkaline media than neutral condition. The release ability of the UIN and G-UIN particles in the acidic and alkaline solutions is more than UIO. The lower Zr and organic compounds concentrations in the extracted solution of G-UIN/EP compared with the UIN sample in the acidic and alkaline pHs indicated more water stability of the modified UIN than UiO [91, 94, 95]. These results prove the smart pH-sensitive controlled release activity of the corrosion inhibitors (Zr ions and organic compounds) from the prepared Zr-MOFs.

Table 1

3.2 Detailed electrochemical explorations

3.2.1 Corrosion simulation

The EIS data were simulated to better understand the mechanism of electrochemical behavior. The Nyquist and Bode plots are presented. The Bode plot consists of the two plots in one plot, the first is the logarithm of the absolute impedance (|Z|), and the second is the phase angle (θ) versus the frequency. To extract the important electrochemical elements from the Nyquist/Bode plots, the fitting of the plots via the electrical models was carried out. The $R(QR)$, $R(Q(R(QR)))$ and $(R(QR)(QR))$ were employed for this simulation. The reliability of the employed EEC models was confirmed by the goodness of fitted data (Pearson χ^2) less than 10^{-3} for all simulations. The EEC models are presented in **Figure 6**. Due to the non-uniformity of the surface of the samples, the pure capacitor (C) was replaced by constant phase element (CPE) derived from the heterogeneity index exponent (n) and admittance (Q) to obtain a good matching between the experimental and fitting data. The CPE_f (related to the film) and CPE_{dl} (related to the double layer) parameters are analyzed. Other important elements extracted by EEC modeling are the resistance of the saline

solution (R_s), inhibitive films (R_f), and charge-transfer (R_{ct}), the admittance of the film (Q_f) and double layer (Q_{dl}) and exponent of the film (n_f) and double layer (n_{dl}). The total resistance is defined as $R_t=R_f+R_{ct}$ that is a good parameter in the electrochemical study. The barrier potency of the intact organic coatings and/or the self-healing and inhibitive film formation ability of the scratched coating was assessed by the log $|Z|_{10\ mHz}$ and $\theta_{10\ KHz}$ parameters [45].

Figure 6

3.2.2 Corrosion studies (solution phase)

Mild steel samples exposed (with the exposed dimension of 1cm×1cm) to the solutions with the MOFs extracts were investigated by EIS after 2, 5, 7, 9, and 24 h of exposure times and compared with the unexposed sample. The samples subjected to the solutions without inhibitors and with UIO, UIN, and G-UIN particles extracts were named as Blank, UIO, UIN, and G-UIN, respectively. The EIS achievements were analyzed by the EECs models. **Figure 7** and **Figure S4** demonstrate the Bode/Nyquist diagrams consisting of fitting/experimental results. The EECs extracted elements from the fitted experimental data are presented in **Table S**2. It was observed that a one-time constant EEC model fits the Blank sample experimental data at all immersion times, but the UIO, UIN, and G-UIO's experimental data were fitted better by the two-time constant EEC models almost in all immersion times. According to the results, it can be seen that log $|Z|_{10\ mHz}$ in the Bode plot and also the diameter of the Nyquist semi-circles (R_t) for the Blank sample change negligible during the times, but for the UIO, UIN and G-UIN sample the log $|Z|_{10\ mHz}$ and R_t increased to higher values by the time, indicating the organic species and Zr ions (released from MOFs) interactions with the metal surface. The low value of R_t (1341 $\Omega.cm^2$) for

Blank sample compared with the higher value of this parameter for UIO (2716 Ω.cm^2), UIN (3192 Ω.cm^2) and G-UIN (2719 Ω.cm^2) samples after 24 h exposure is strong evidence proving the inhibition effect of Zr and organic compounds released from the MOFs. For the Blank sample, the reactions that occur on the corrosion sites are controlled by charge transfer with the heterogeneous surface (n_{dl}). Unlike the Blank sample, the higher values of the heterogeneity index exponent (n_{dl}) for UIO, UIN, and G-UIN particles are good evidence for homogeneity of the inhibited films generated on the metal surface. This observation shows non-porous inhibited barrier films on the sample subjected to the MOFs containing extract [96].

Figure 7

The corrosion inhibition, as well as the mechanism of the Blank, UIO, UIN, and G-UIN samples, was assessed by potentiodynamic polarization analysis after 9 h exposure (**Figure 8)**. **Table S**3 presents the anodic (i_a) and cathodic (i_c) Tafel slopes, potential (E_{corr}), and current density (i_{corr}) of corrosion state extracted by Tafel-extrapolation approach. According to the result, all samples exhibited good anti-corrosion capability with compared to Blank sample, but the best anti-corrosion behavior (the lower corrosion rate) was evidenced for the UIO sample by the lowest i_{corr} (2.84 μA/cm^2) and E_{corr} (-727.19 V/SCE) values, compared with the Blank (i_{corr}=5.06 μA/cm^2, E_{corr}= -687.5 V/SCE) sample. Due to the greater variation of the cathodic Tafel slope of UIO (−0.142 V/dec), UIN (−0.165 V/dec) and G-UIN (−0.187 V/dec) sample with compared to the Blank sample (−0.234 V/dec), the released Zr cations and organic ligand molecules from the MOFs mainly react with the OH^- spices and Fe^{2+} cations generated on the cathodic and anodic zones respectively, causing the creation of an inhibitive protective film on these regions [97, 98].

Figure 8

3.2.3 Active (self-healing) corrosion protection evaluation of scratched epoxy composites

The active corrosion protection properties of the EP, UIO/EP, UIN/EP and G-UIN/EP samples (with the exposed dimension of 2 cm × 2 cm) with an artificial defect (with a scratch length of 1 cm) were studied by EIS at exposure times of 4, 6, 8 and 24 h. **Figure 9** and **Figure S5** respectively show the Nyquist diagrams and Bode plots. The EP experimental data and the UIO/EP, UIN/EP, and G-UIN/EP samples experimental data were well fitted through (R(QR)(QR)) and (R(Q(R(QR)))) EEC models, respectively. The EECs extracted parameters from the fitted experimental data are presented in **Table S4**. For EP, the diameter of the Nyquist semi-circles decreased with time. It is evident that the log $|Z|_{10\ mHz}$ value for EP in the Bode plot decreases from 4.59 Ω.cm^2 to 4.15 Ω.cm^2 after 24 h, respectively. As said, the experimental data of the EP sample was fitted with the series modes of two time-constant EEC models due to the porous film formation within the scratched zone. The lower amount of the heterogeneity index exponent (n_{dl}) is good evidence for this fact. For the EP sample, the total value of resistance (R_t) shows a descending trend as the immersion time progressed and reached the lowest value of about 15773 Ω.cm^2 at 24 h. Due to the formation of unstable and porous films within the scratch zone, the corrosive materials such as water, $Cl^{-,}$ and O_2 could diffuse into the scratched area. The electrochemical reactions progress in the presence of corrosive materials and cause loss of the metal/coating interfacial bonding, leading to the penetration of the developed iron oxidized product into the interface of polymer/steel, and as a result, the coating delamination occurs. Unlike the EP, the Nyquist diagrams diameter of semi-circles and also the log $|Z|_{10\ mHz}$ increased with the immersion time progress and finally decreased. In addition, the R_t value for the UIO/EP, UIN/EP, and G-UIN/EP samples increased up to 24 h exposure and then decreased to 33291, 58732, 60077 Ω.cm^2, respectively that are much more than the R_t value for EP sample. The increase of the diameter of the Nyquist semi-circles, the log $|Z|_{10\ mHz}$, and R_t are good evidence demonstrating the active

inhibitive corrosion retardation action of the UIO, UIN, and G-UIN particles reinforced coatings. Unlike the UIO/EP and UIN/EP samples, the values of R_t and log $|Z|_{10\ mHz}$ for G-UIN/EP are more than other samples, showing the good active corrosion protection performance that is related to the inhibitors controlled release behavior as well as the metal/coating interfacial adhesion bonding promotion [99].

Figure 9.

3.2.4 Corrosion study of the intact EP, UIO/EP, UIN/EP, and G-UIN/EP samples

The barrier performance of the EP, UIO/EP, UIN/EP, and G-UIN/EP samples were studied by EIS in the saline solution after exposure times of 2, 63, 84, 98, and 120 days. **Figure 10** and **Figure S6** show the Bode (phase, modulus)/Nyquist plots. The experimental EIS data corresponded to the EP, UIO/EP, and G-UIN/EP samples were fitted by (R(QR)) model, but it was observed that the (R(Q(R(QR)))) model better fitted the UIN/EP data after 84, 98 and 120 days of immersion. The data are collected in **Table S**5. The log $|Z|_{10\ mHz}$ (2 days) of the EP, UIO/EP, UIN/EP, and G-UIN/EP samples were more than 10 Ω.cm^2, reflecting superior barrier protection of all samples for a short time of NaCl subjection. But, the log $|Z|_{10\ mHz}$ of the EP samples decreased drastically to 7.55 Ω.cm^2 after 120 days exposure, illustrating the degradation of the unfilled (neat) EP by the immersion of the EP sample in the saline solution. The UIN/EP sample was believed to indicate acceptable barrier property in comparison with the neat-EP, but the result showed that the log $|Z|_{10\ mHz}$ values for 63, 84, 98, and 120 days is less than the EP sample. The new time-constant observed at the low-range f in the phase angle plots of the UIN/EP sample after 84 days of NaCl subjection reveals the acceleration of the corrosion product and/or the inhibitive film formation at the

coating/steel interfaces. The results showed good barrier property of the UIO/EP than the UIN/EP and EP samples. Results reveal the superior barrier potency of the G-UIN/EP than the EP, UIO/EP, and UIN/EP ones. The log $|Z|_{10\ mHz}$ magnitudes of the G-UIN/EP sample are more than about 10.0 $\Omega.cm^2$ even after 98 days that shows excellent barrier properties of the G-UIN/EP sample. According to the Bode plot, the impedance diagrams for the G-UIN/EP sample showed capacitive behavior in the range of the frequency up to 98 days, proving the excellent barrier potency of the coating [100].

Figure 10.

The EP, UIO/EP, UIN/EP, and G-UIN/EP samples protection capacity evaluation can be further done by determining the breakpoint frequency (f_b) values from the Bode plots. The values of the f_b are presented in **Figure S7**. The f_b value can be extracted from the Bode phase angle plot (**Figure 10-a**), elucidating the f at $\Theta=-45°$. The corrosion protectiveness and also coating disbonding area are related to the f_b magnitude [101]. The log (f_b) values for the EP, UIO/EP, and UIN/EP composites are -1.2, -1.88 and -1.9 Hz after 2 days of immersion, respectively, but no breakpoint frequency was observed for G-UIN/EP sample until 63 days, indicating the superior protection potency of the coating reinforced with the G-UIN particles. The values of log (f_b) at 120 h of immersion time increased to 1.03, − 0.53, 1.17, and −1.42 for the EP, UIO/EP, UIN/EP, and G-UIN/EP samples, respectively. The positive log (f_b) magnitudes for the EP and UIN/EP samples show the decreased coating (EP) capacitive behavior resulted from the electrolyte penetration and oxidized iron product generation/diffusion into the metal/epoxy interface, causing the loss of adhesion. Unlike the EP and UIN/EP samples, the more negative value of the G-UIN/EP sample is due to the superior barrier property and/or good adhesion at metal/coating interfaces of this sample with compared to others [8, 102].

Another theoretical approach to determine the coatings protection ability is the intersection of the Bode plot (IBP). There is an interconnection between the intersection of the Bode plot and coatings properties [103]. This value was extracted by the intersected point of Bode-ϴ plots and Bode-|Z| impedance plot that is related to the corrosion protection behavior and barrier property. The shift of the frequency of the IBP to the higher frequencies is connected to the electrolyte uptake into the degraded coating [8]. The intersection values of the EP, UIO/EP, UIN/EP, and G-UIN/EP samples (versus time) are given in **Figure S8**. According to the results, as the exposure time elapsed, the IBP of the epoxy and UIN/EP samples remarkably displaced to the higher *f* values, indicating the water, O_2, and the diffusion of the corrosive ions into the structure of the coatings. The IBPs of the UIO/EP and G-UIN/EP are far less than the IBP value of the EP and the UIN/EP samples, evidencing the decrease of the diffusion rate of water (including ions) and O_2 into the coating by adding the UIO and G-UIN particles.

The coating with an excellent barrier property shows capacitive behavior in all frequency ranges between 10^{-2}-10^{4} Hz. As the electrochemical reactions began under the metal/coating interface, the breakpoint frequency appears, and the Bode modulus plot can be divided into two characteristic resistive and capacitive regions with different slopes of 0 and −1, respectively. The ions/water penetration into the coating leads to the decrease of the capacitive region that is related to coating structure damage. The broadening of the resistive (slope=0) region is related to the coating degradation that happened on the metal/coating interfaces. Besides, the changes of the resistive and capacitive areas under the Bode plot are other good parameters to determine the delamination extent of the intact coating with the immersion time progress. The coating undamaged index was defined by **Eq (1)** [102].

$$\text{Coating Undamaged Index } (\%) = \left(\frac{A_2}{A_1}\right)\times 100 \qquad \text{eq (1)}$$

A_1 and A_2 (the calculated area from the capacitive part of the plot) are describing the undamaged (2 days) and damaged (120 days) coatings, respectively. The determination way of the resistive/capacitive regions in the Bode plot is introduced in **Figure S9,** and the results are given in **Figure S10**. The undamaged indexes for the EP, UIO/EP, UIN/EP, and G-UIN/EP samples are 46.90, 69.31, 34.60, and 85.93 %, respectively, indicating the high barrier properties and less damaged metal/coating interfacial bonding of UIO/EP and G-UIN/EP samples. The coating undamaged index values are clearly in the strong agreement with the other results obtained in the barrier property study [104].

Corrosion study of the intact EP, UIO/EP, UIN/EP, and G-UIN/EP samples revealed excellent barrier properties for UIO/EP and G-UIN/EP samples. But, the weak barrier protection behavior was obtained for the EP and UIN/EP samples. There are some reasons for the EP sample barrier property decline with the exposure time progress. Some unavoidable inhomogeneities such as microscopic pores and defects, weak and nonbonded areas of metal substrate/coating interfacial, microvoids, cracks, and air bubbles may be formed during the EP curing process on the steel substrate, that leads to the electrolyte penetration into the EP coating. The electrolyte (NaCl) diffusion into the microscopic-pores/defects during the time causes the EP barrier potency decline [105]. Some of the microscopic pores and defects may be barricaded by adding the UIO, UIN, and G-UIN particles. In addition, adding the particle could affect the curing of the epoxy coating, improving the barrier effect. Good dispersion of the UIO and G-UIN particles in the epoxy polyamide coating is a major mechanism to improve the barrier property of the UIO/EP and G-UIN/EP samples. Surface treatment of the UIN by GMA led to excellent barrier properties. The result shows that adding the UIN particles to the EP leads to the loss of barrier properties. The NH_2 groups' presence on the outer surface of the UIN particles could create chemical-bonding through

the ring-opening mechanism by reaction with the epoxy groups of the resin. Due to this fact, it had been expected that adding the UIN particles to the epoxy coating leads to the enhancement of the barrier effect, but as the results showed, adding the UIN particles to the epoxy coating not only didn't improve the barrier property but also decreased it. The interference and competition between the hardener and NH_2 groups of the UIN particles may lead to the destruction of the curing process and as a consequent decline in the barrier properties of the coating [28, 60].

3.3 Corrosion study of the coatings by SST

To assess the effectiveness of the UIO, UIN, and G-UIN particles in the epoxy coating, the SST was done on the scratched coated samples. The appearance of the scratched EP, UIO/EP, UIN/EP, and G-UIN/EP coated samples before (that is named 0), and after 10 and 20 days of exposure to the SST chamber are presented at in **Figure 11**. The visual performance of the EP sample reflects its delamination after 10 days of SST exposure that is due to the electrolyte and Fe-oxide product penetration into the EP/steel interface. The UIO/EP and UIN/EP samples showed acceptable corrosion protection behavior until 10 days, and the delaminated area is very low. The corrosion protection of the UIO/EP sample decreased after 20 days. There is some blister in the non-scratched zone of the UIN/EP after 10 days of SST, representing the weakness of the water-barrier capability and/or adhesion of the UIN/EP sample that is in good agreement with the intact corrosion study achievements. As it was believed, the G-UIN/EP sample showed excellent corrosion property even up to 20 days of SST and no significant delamination around the scratched zone and also no blister in the non-scratched zone can be seen.

Figure 11

3.4 Adhesion measurements

The adhesion properties of the dry and wet EP, UIO/EP, UIN/EP, and G-UIN/EP samples were studied by a pull-off test on the coated samples before and after 14 days of exposure to the SST accelerated chamber. The optical appearance of the samples after the pull-off analysis is shown in **Figures 12-13**. The adhesion strength loss (ASL %) of the sample was calculated by Eq (1) [106].

$$ASL\ (\%) = \left(\frac{\Gamma_D - \Gamma_W}{\Gamma_D}\right) \times 100\ \% \qquad \text{eq (2)}$$

In the above equation, Γ_D and Γ_W are describing the dry-adhesion and wet-adhesion magnitudes, respectively. The calculated ASL % results for the EP, UIO/EP, UIN/EP, and G-UIN/EP samples are shown in **Figure S11**. According to the results, incorporation of the MOFs into the EP coating causes significant coating adhesion enhancement. The optical appearance of the EP sample after the pull-off test shows adhesion loss in both dry-(before exposure to NaCl) and wet (exposed samples) conditions. The delaminated region of the EP sample in the wet condition is the most significant. The calculated adhesion strength loss (ASL %) for the EP sample is about 48 %. The UIO/EP, UIN/EP, and G-UIN/EP samples showed superior adhesion properties in the dry condition, but for the UIN/EP sample, an insignificant cohesive failure was observed. In the wet condition, the insignificant cohesive failure of UIO/EP and also adhesive strength loss of the UIN/EP samples were observed. The ASL values of 35% and 22.4% were calculated using the dry-adhesion and wet-adhesion data achieved by the pull-off test for the UIO/EP and UIN/EP specimens, respectively. The lower value of the ASL (21.1 %) is observed for the G-UIN/EP sample, and no adhesive loss and cohesive failure were observed from the optical appearance of the G-UIN/EP sample, indicating the superior interfacial bonds at the metal substrate/coating interface and good G-UIN particles distribution/dispersion in the EP matrix.

Figure 12

3.5 Wet adhesion study of the coatings through CDT

Although the selection of an appropriate organic coating guarantees the metal substrate protection in front of aggressive environments in the insensitive application, in some specific applications, it could not guarantee the long time protection of the metal substrate. To overcome this problem, a combination of the organic coating systems and cathodic protection is suggested. The cathodic disbondment test (CDT) is the loss of wet adhesion at the metal substrate/coating interface caused by an impressed cathodic protecting current. CDT interferes with the corrosion process and protects the metal substrate [107]. But all of these unique performance losses once the defect or mechanical damage creates on the coatings, and CDT may backfire due to the weakness of the adhesion between the metal/coating interfaces. In the CDT, the hydroxyl radicals generate and react with Na^+, resulting in the increases of pH even to the high alkaline pH. It is not unexpected that the organic coatings might be degraded under these acute conditions. Chain scission, saponification, and hydrolysis of the metal/coating interaction are the unavoidable processes in the high alkaline pH for most of the organic coatings [108]. To overcome this problem, the improvement of the metal/coating interfacial adhesion is necessary [109]. In this study, the wet adhesion of the epoxy polyamide coated specimens without particles and with MOFs were studied by CDT according to the method that previously mentioned. The digital image of the samples after CDT and disbonding radius values were presented in **Figure 12** and **Figure 13,** respectively. The delamination radiuses of the unfilled epoxy, UIO/EP, UIN/EP, and G-UIN/EP samples are about 14.86, 9.42, 10 and 8.02 mm, respectively. According to the result, the MOFs particles loading into the coating led to the decrease of the delamination radius values and improvement of the adhesion strength of about 36.6, 32.7 and 46 %, respectively. The adhesion enhancement of the metal/coating interfacial bonds and/or the decrease of the pH value at the metal/coating interface

are two main important reasons for these results. As before said, the partial dissolution of the MOFs leads to the release of the Zr cations. The released Zr ions react with the generated OH^- radicals on the metal surfaces and neutralize the alkaline pH and/or block the cathodic zone on the metal surface. The G-UIN/EP sample showed the lowest delamination radius evidencing the controlled Zr ions release from the G-UIN and also good dispersion of the G-UIN particles in the EP coating. The UIN/EP sample shows the disbonding radius value more than the UIO/EP and G-UIN/EP that may be due to the microscopic defect generation by UIN particles within the disruption of the epoxy-polyamide curing process.

Figure 13

3.6 Surface analysis

FE-SEM micrographs conjugated EDS map analysis was conducted for the EP, UIO/EP, UIN/EP, and G-UIN/EP samples to study the composition and morphology of corrosion products generated within the scratch region after 20 days of exposure to the SST (**Figure 14)**. The inhibitive uniform film generated within the scratched region after SST was observed for the UIO/EP, UIN/EP, and G-UIN/EP samples. Non-uniform deposition of the porous film within the scratch region indicates the unstable generation of corrosion products. The FE-SEM images showed distinct uniform and dense inhibitive film deposited within the scratch zone for G-UIN/EP with compared to the other samples, resulting in more corrosion protection property and lower delaminated area for the coated samples. The chemical compositions of the deposited inhibitive film within the scratch are shown in **Table S**6. As mentioned before, although the synthesized MOFs in this paper behave high stability in the water in the neutral condition, our study illustrates the partial dissolution and/or degradation of the UIO, UIN, and G-UIN [53, 94]. The EDS results showed the presence of Zr ions and N atoms within and the surrounding area of the scratch for the UIO/EP, UIN/EP, and G-

UIN/EP samples. Detection of the Zr ions and N atoms in the EDS results is good evidence for the inhibitive film formation within the scratch region. The film formation mechanisms were explained before [110].

Figure 14

3.7 Corrosion protection mechanisms

As mentioned before, the cathodic and anodic reactions start as soon as water, O_2, Na^+, and chloride ions penetration as corrosive species into the interface of metal/coating. The hydroxyl radicals and Fe^{2+} ions (or Fe^{3+}) are the results of the cathodic and anodic reactions, respectively. OH^- and Fe^{2+} (or Fe^{3+}) could react with the diffused Na^+ and Cl^- and produce NaOH and hydrated ferrite species, resulting in the high alkaline and low acidic pH zones on the metal surface, respectively. The organic coatings adhesion bonds to the metal surface might be degraded under these acute conditions. The loss of the barrier effect of the EP sample might be due to the chain scission, saponification, and hydrolysis of the metal/coating interactions in the high alkaline and low acidic pHs during the time. The water stability results showed a smart controlled release activity of the corrosion inhibitors (Zr ions and organic compounds) from UIO, UIN, and G-UIN. According to the ICP and TOC results, the high stability of the synthesized Zr-MOF was obtained in the neutral condition, but the increment of the release ability of the Zr-MOFs was observed in the high alkaline and low acidic pHs. This interesting observation help to find the corrosion protection mechanisms of the epoxy coatings incorporated with the UIO, UIN, and G-UIN particles. As the corrosive species penetrate into the interface of metal/coating, the high alkaline, and low acidic pH zones can be generated on the metal surface, and the Zr-MOF particles connected to the metal surface start to degradation. As before said, the partial dissolution of the Zr-MOFs leads to the release of the Zr cations and organic compounds. The released Zr ions and organic compounds react with the generated OH^- ions and Fe^{2+} on the metal surfaces, respectively,

and neutralize the alkaline pH and/or block the cathodic and anodic zones on the metal surface [45]. That is the way that the coated metal could be protected in the intact and scratch forms by adding the Zr-MOFs particles to the epoxy coating.

3.8 Hardness measurements

Coating's resistance to permanent deformation is defined as a hardness. In this study, Vickers micro-hardness, Pendulum (Konig) Hardness, and scratch test were conducted according to the test method mentioned previously, to assess the coating hardness and resistance to the scratch and penetration. The Vickers micro-hardness test was carried out on the EP, UIO/EP, UIN/EP, and G-UIN/EP samples, and the morphology of the Vickers indent and the extracted data are shown at **Figure 15** and **Table 2**, respectively. As results show, the Vickers hardness (MPa) values (and Diagonal lengths (mm)) for the EP, UIO/EP, UIN/EP, and G-UIN/EP samples are about 0.98 (442.6), 1.96 (284.2), 0.99 (343.1), and 1.96 (275.1), respectively. To assess the coating's resistance to scratch, the scratch test was done, and the values of loading for the EP, UIO/EP, UIN/EP, and G-UIN/EP samples were about 1550 kg, 1600 kg, 1660 kg, and 1700 kg, respectively. The optical image for this test is shown in **Figure S12**. Konig Hardness test results for the EP, UIO/EP, and UIN/EP and G-UIN/EP samples are between about 154-160 seconds, and no significant change was observed for the Konig hardness by adding of the MOFs particle to the epoxy coating. The results of the hardness of the coatings showed that incorporation of the UIO, UIN, and G-UIN particles into the epoxy coating could improve the coating's resistance against scratch and penetration [111, 112].

Figure 15

Table 2

3.9 Complexes adsorption

The adsorption of Zr^{+4} complexes containing organic linkers of bare/modified terephthalic acid was modeled in gas medium (via MC) and in liquid/aqueous electrolyte with MD. The configurations modeled by MC type simulation were graphically demonstrated in **Figure 16**. The visualized pictures seemingly show that all three Zr^{+4}/terephthalic acid, Zr^{+4}/2-amino-terephthalic acid, and Zr^{+4}/GMA-bonded 2-amino-terephthalic acid complexes stayed next to the substrate after MC simulations. This surface adherence denotes the surface binding nature of zirconium (IV) complexes. It is clearly noticed that the Zr^{+4} complexes with a lower number of organic linkers (i.e., smaller complexes) accepted a completely planar arrangement. However, some ligands in the two largest complexes (i.e., n=5 and 6) stabilized at farther distances from the substrate. Various kinds of energetics related to visualized MC configurations were prepared in **Table S**7. The adsorption energies pertaining to studied zirconium (IV)/organic complexes possessed negative sign, an MC-derived observation evidencing the spontaneous interfacial adsorptivity onto target adsorbent.

Figure 16

The final aqueous-phase cells simulated by MD type dynamics modeling were portrayed in **Figure 17** for evaluated inorganic/organic complex compounds. The extracted snapshots visually declare that the cationic metal (i.e., zirconium (IV))/organic (based on unmodified/modified terephthalic acid) complex compounds kept their affinity for adsorbing on the considered crystalline substrate which is in contact with solvent molecules. Careful evaluation of the interface ensures that the parallel mode adsorption was almost preserved over the water-solvated metallic adsorbent. The MD-suggested snapshots were studied from a quantitative point of view for which the adsorption energy of each specific snapshot was estimated [113]. It was understood that the $[Zr(TA)_2]^{+4}$,

$[Zr(TA)_3]^{+4}$, $[Zr(TA)_4]^{+4}$, $[Zr(TA)_5]^{+4}$, and $[Zr(TA)_6]^{+4}$ adsorption owned the -1082.9, -1135.0, -1175.4, -1091.9, and -1143.8 kcal/mol energy, respectively. For the adsorbed $[Zr(ATA)_2]^{+4}$, $[Zr(ATA)_3]^{+4}$, $[Zr(ATA)_4]^{+4}$, $[Zr(ATA)_5]^{+4}$, and $[Zr(ATA)_6]^{+4}$ complexes, the energies (kcal/mol) of -1099.3, -1184.1, -1299.5, -1303.5, and -1271.6 were respectively elucidated. Also, the adsorption of $[Zr(GMA\text{-}ATA)_2]^{+4}$, $[Zr(GMA\text{-}ATA)_3]^{+4}$, $[Zr(GMA\text{-}ATA)_4]^{+4}$, $[Zr(GMA\text{-}ATA)_5]^{+4}$, and $[Zr(GMA\text{-}ATA)_6]^{+4}$ complexes respectively accompanied with -1198.5, -1332.1, -1493.4, -1467.4, and -1569.5 kcal/mol energy. The resulting energies (with negative sign) quantitatively support the surface binding feature on the solvated steel surface.

Figure 17

3.10 Electronic features

The reactive complexes sites emerging as adsorption regions relative to metallic adsorbent were theoretically assessed by qualitative/quantitative analysis of molecular orbitals and electron sharing. These features were studied in structurally equilibrated Zr^{+4} complexes given in **Figure 18**. The literature survey highlights that the capacity of the resistive chemical against electron sharing (i.e., donation and acceptance) can be explained with two known orbitals of HOMO and LUMO [114-116]. The graphical outcomes of HOMO and LUMO relevant for Zr^{+4} and bare/modified terephthalic acid complexes were respectively provided in **Figures 6** and **7**. It is noticed that the isosurface for HOMO (**Figure 19**) in different Zr^{+4}/terephthalic acid complexes (namely $[Zr(TA)_n]^{+4}$) distributed above the carboxylic acid moiety and somewhat on ring bonds of one or two terephthalic acid ligands. In 2-amino-terephthalic acid complexation with Zr^{+4}, the aromatic terephthalic acid ring, amine group, and carbonyl type heteroatom of O served as possible HOMO isosurfaces. The HOMO of $[Zr(GMA\text{-}ATA)_n]^{+4}$ complexes is mostly the same as that of $[Zr(ATA)_n]^{+4}$ ones. The distinction is that in smaller complexes, the HOMO is placed on hydroxyl

O and some carbon centers of the GMA side group. Consequently, the sites involved in HOMO isosurface can serve as charge donors and thereby supply electrons (that is, lone pair and π) to suitable electrophiles (i.e., metal layer atoms with empty orbitals).

Figure 18

Figure 19

As exhibited in **Figure 20**, the LUMO of all Zr^{+4} complexes with unmodified/modified terephthalic acid principally distributed over the zirconium (IV) cation and the O atoms directly connected to cation. The isosurface of this orbital is noted to emerge slightly on terephthalic acid ring C atoms. Hence, the main electron-accepting regions of organic/inorganic complexes are the Zr^{+4} cation and neighboring heteroatoms, which are capable of getting electrons given by potential nucleophiles, for instance, the occupied orbitals located in metal atoms. The computed orbitals eigenvalues shared electrons, and other chemical descriptors were collected in **Table S**8. This table proves that the ΔN magnitudes estimated for all zirconium (IV) complexes are negative, emphasizing the preference of these compounds for acceptance of electrons. Additionally, it is obviously seen that with bonding more organic linkers to zirconium cation, the ΔN amounts became less negative, which signifies the weakened electron getting propensity of cationic complexes. This electronic-structure observation can be described by the lowered electron affinity (and electronegativity) of complexes containing more organic ligands. This outcome can be further rationalized by the less negative or higher LUMO eigenvalue of larger complexes clarifying their less intensified electron-accepting tendency.

Figure 20

4. Conclusion

UIO, UIN, and modified UIN (G-UIN) were fabricated as novel Zr-MOF based corrosion inhibitor carriers and investigated through FT-IR, ICP-OES, TGA, XRD, FE-SEM, and solubility test, polarization, and EIS. The electrochemical behaviour and adhesion study of the Zr-MOFs incorporated into the EP was illustrated by EIS, SST, and CDT. The conclusions are summarized below:

1- Accurate fabrication of the UIO, UIN, and G-UIN was illustrated via FT-IR analysis, XRD, TGA, BET, and FE-SEM. The results proved the MOFs successful formation.

2- Partial solubility of the Zr-MOFs was illustrated through Zr cations release in the extracted solution by ICP-OES.

3- The active-barrier protection ability of the Zr-MOFs incorporated EP was demonstrated by electrochemical analyses achievements. The results showed superior inhibition action and water/ions barrier capability of the EP containing the G-UIN (G-UIN/EP) sample.

4- The incorporation of the UIO, UIN, and G-UIN particles into the EP matrix led to the metal/coating interfacial adhesion enhancement. The lowest value of the delamination radius belonged to the G-UIN/EP sample that is connected to the appropriate level of the G-UIN particle dispersion in the coating.

5- The incorporation of the UIO, UIN, and G-UIN particles into the epoxy coating improved the hardness and coating's resistance to the scratch and penetration.

6- The detailed-scale DFT complemented with MC/MD inspections theoretically ensured the great affinity of coordination compounds for adsorption on the target steel type substrate.

References

[1] M. Chigondo, F. Chigondo, Recent natural corrosion inhibitors for mild steel: an overview, Journal of Chemistry, 2016 (2016), 1-7.
[2] W. Li, B. Ren, Y. Chen, X. Wang, R. Cao, Excellent Efficacy of MOF Films for Bronze Artwork Conservation: The Key Role of HKUST-1 Film Nanocontainers in Selectively Positioning and Protecting Inhibitors, ACS applied materials & interfaces, 10 (2018) 37529-37534.
[3] G. Grundmeier, A. Simões, Corrosion protection by organic coatings, Encyclopedia of Electrochemistry: Online, (2007).
[4] F.-L. Jin, X. Li, S.-J. Park, Synthesis and application of epoxy resins: A review, Journal of Industrial and Engineering Chemistry, 29 (2015) 1-11.
[5] M. Kasaeian, E. Ghasemi, B. Ramezanzadeh, M. Mahdavian, G. Bahlakeh, A combined experimental and electronic-structure quantum mechanics approach for studying the kinetics and adsorption characteristics of zinc nitrate hexahydrate corrosion inhibitor on the graphene oxide nanosheets, Applied Surface Science, 462 (2018) 963-979.
[6] S. Mousavifard, P.M. Nouri, M. Attar, B. Ramezanzadeh, The effects of zinc aluminum phosphate (ZPA) and zinc aluminum polyphosphate (ZAPP) mixtures on corrosion inhibition performance of epoxy/polyamide coating, Journal of Industrial and Engineering Chemistry, 19 (2013) 1031-1039.
[7] X. Cao, F. Huang, C. Huang, J. Liu, Y.F. Cheng, Preparation of graphene nanoplate added zinc-rich epoxy coatings for enhanced sacrificial anode-based corrosion protection, Corrosion Science, 159 (2019) 108120.
[8] B. Ramezanzadeh, E. Ghasemi, M. Mahdavian, E. Changizi, M.M. Moghadam, Covalently-grafted graphene oxide nanosheets to improve barrier and corrosion protection properties of polyurethane coatings, Carbon, 93 (2015) 555-573.
[9] M. Motamedi, M. Ramezanzadeh, B. Ramezanzadeh, M. Mahdavian, One-pot synthesis and construction of a high performance metal-organic structured nano pigment based on nanoceria decorated cerium (III)-imidazole network (NC/CIN) for effective epoxy composite coating anti-corrosion and thermo-mechanical properties improvement, Chemical Engineering Journal, 382 (2020) 122820.
[10] R.G. Buchheit, H. Guan, S. Mahajanam, F. Wong, Active corrosion protection and corrosion sensing in chromate-free organic coatings, Progress in Organic Coatings, 47 (2003) 174-182.
[11] B. Ramezanzadeh, M. Attar, M. Farzam, A study on the anticorrosion performance of the epoxy–polyamide nanocomposites containing ZnO nanoparticles, Progress in Organic Coatings, 72 (2011) 410-422.
[12] N. Asadi, R. Naderi, M. Mahdavian, Doping of zinc cations in chemically modified halloysite nanotubes to improve protection function of an epoxy ester coating, Corrosion Science, 151 (2019): 69-80.

[13] S.A. Haddadi, A. Ramazani SA, M. Mahdavian, P. Taheri, J.M. Mol, Mechanical and corrosion protection properties of a smart composite epoxy coating with dual-encapsulated epoxy/polyamine in carbon nanospheres, Industrial & Engineering Chemistry Research, 58.8 (2019): 3033-3046.
[14] Q. Zhu, W. Zhuang, Y. Chen, Z. Wang, B. Villacorta Hernandez, J. Wu, P. Yang, D. Liu, C. Zhu, H. Ying, Nano-biocatalysts of Cyt c@ ZIF-8/GO composites with high recyclability via a de novo approach, ACS applied materials & interfaces, 10 (2018) 16066-16076.

[15] J. Wang, Y. Wang, Y. Zhang, A. Uliana, J. Zhu, J. Liu, B. Van der Bruggen, Zeolitic imidazolate framework/graphene oxide hybrid nanosheets functionalized thin film nanocomposite membrane for enhanced antimicrobial performance, ACS applied materials & interfaces, 8 (2016) 25508-25519.
[16] C. Li, C. Hu, Y. Zhao, L. Song, J. Zhang, R. Huang, L. Qu, Decoration of graphene network with metal–organic frameworks for enhanced electrochemical capacitive behavior, Carbon, 78 (2014) 231-242.
[17] Y.-P. Wu, X.-Q. Wu, J.-F. Wang, J. Zhao, W.-W. Dong, D.-S. Li, Q.-C. Zhang, Assembly of Two Novel Cd3/(Cd3+ Cd5)-Cluster-Based Metal–Organic Frameworks: Structures, Luminescence, and Photocatalytic Degradation of Organic Dyes, Crystal Growth & Design, 16 (2016) 2309-2316.
[18] S.R. Batten, S.M. Neville, D.R. Turner, Coordination polymers: design, analysis and application, Royal Society of Chemistry, 2008.
[19] P. Silva, S.M. Vilela, J.P. Tomé, F.A.A. Paz, Multifunctional metal–organic frameworks: from academia to industrial applications, Chemical Society Reviews, 44 (2015) 6774-6803.
[20] P. Cheng, M. Bosch, Lanthanide metal-organic frameworks, Springer, 2015.
[21] O.K. Farha, I. Eryazici, N.C. Jeong, B.G. Hauser, C.E. Wilmer, A.A. Sarjeant, R.Q. Snurr, S.T. Nguyen, A.O.z.r. Yazaydın, J.T. Hupp, Metal–organic framework materials with ultrahigh surface areas: is the sky the limit?, Journal of the American Chemical Society, 134 (2012) 15016-15021.
[22] A.U. Czaja, N. Trukhan, U. Müller, Industrial applications of metal–organic frameworks, Chemical Society Reviews, 38 (2009) 1284-1293.
[23] K.K. Gangu, S. Maddila, S.B. Mukkamala, S.B. Jonnalagadda, A review on contemporary Metal–Organic Framework materials, Inorganica Chimica Acta, 446 (2016) 61-74.
[24] P. Kumar, V. Bansal, A. Paul, L.M. Bharadwaj, A. Deep, K.-H. Kim, Biological applications of zinc imidazole framework through protein encapsulation, Applied Nanoscience, 6 (2016) 951-957.
[25] H.-L. Wang, H. Yeh, Y.-C. Chen, Y.-C. Lai, C.-Y. Lin, K.-Y. Lu, R.-M. Ho, B.-H. Li, C.-H. Lin, D.-H. Tsai, Thermal Stability of Metal–Organic Frameworks and Encapsulation of CuO Nanocrystals for Highly Active Catalysis, ACS applied materials & interfaces, 10 (2018) 9332-9341.
[26] S. Yuan, L. Feng, K. Wang, J. Pang, M. Bosch, C. Lollar, Y. Sun, J. Qin, X. Yang, P. Zhang, Stable metal–organic frameworks: design, synthesis, and applications, Advanced Materials, 30 (2018) 1704303.
[27] W. Xu, X. Wang, Y. Wu, W. Li, C. Chen, Functionalized graphene with Co-ZIF adsorbed borate ions as an effective flame retardant and smoke suppression agent for epoxy resin, Journal of hazardous materials, 363 (2019) 138-151.
[28] C. Liu, M. Mullins, S. Hawkins, M. Kotaki, H.-J. Sue, Epoxy Nanocomposites Containing Zeolitic Imidazolate Framework-8, ACS applied materials & interfaces, 10 (2017) 1250-1257.
[29] H. Tian, W. Li, A. Liu, X. Gao, P. Han, R. Ding, C. Yang, D. Wang, Controlled delivery of multi-substituted triazole by metal-organic framework for efficient inhibition of mild steel corrosion in neutral chloride solution, Corrosion Science, 131 (2018) 1-16.
[30] S. Kumaraguru, R. Pavulraj, S. Mohan, Influence of cobalt, nickel and copper-based metal-organic frameworks on the corrosion protection of mild steel, Transactions of the IMF, 95 (2017) 131-136.

[31] A. Mesbah, C. Juers, F. Lacouture, S. Mathieu, E. Rocca, M. François, J. Steinmetz, Inhibitors for magnesium corrosion: metal organic frameworks, Solid State Sciences, 9 (2007) 322-328.
[32] M. Zhang, L. Ma, L. Wang, Y. Sun, Y. Liu, Insights into the Use of Metal–Organic Framework As High-Performance Anticorrosion Coatings, ACS applied materials & interfaces, 10 (2018) 2259-2263.
[33] A.E.-A.S. Fouda, S.E.-D.H. Etaiw, M.M. El-bendary, M.M. Maher, Metal-organic frameworks based on silver (I) and nitrogen donors as new corrosion inhibitors for copper in HCl solution, Journal of Molecular Liquids, 213 (2016) 228-234.
[34] S.E.-d.H. Etaiw, A.E.-A.S. Fouda, S.A. Amer, M.M. El-bendary, Structure, characterization and anti-corrosion activity of the new metal–organic framework [Ag (qox)(4-ab)], Journal of Inorganic and Organometallic Polymers and Materials, 21 (2011) 327-335.
[35] S.E.-d.H. Etaiw, A.E.-A.S. Fouda, S.N. Abdou, M.M. El-bendary, Structure, characterization and inhibition activity of new metal–organic framework, Corrosion Science, 53 (2011) 3657-3665.
[36] H. Ji, S. Hwang, K. Kim, C. Kim, N.C. Jeong, Direct in Situ Conversion of Metals into Metal–Organic Frameworks: A Strategy for the Rapid Growth of MOF Films on Metal Substrates, ACS applied materials & interfaces, 8 (2016) 32414-32420.
[37] N.C. Burtch, H. Jasuja, K.S. Walton, Water stability and adsorption in metal–organic frameworks, Chemical reviews, 114 (2014) 10575-10612.
[38] H. Zhang, M. Zhao, Y. Lin, Stability of ZIF-8 in water under ambient conditions, Microporous and Mesoporous Materials, 279 (2019): 201-210.
[39] C. Wang, X. Liu, N.K. Demir, J.P. Chen, K. Li, Applications of water stable metal–organic frameworks, Chemical Society Reviews, 45 (2016) 5107-5134.
[40] M. De Toni, R. Jonchiere, P. Pullumbi, F.X. Coudert, A.H. Fuchs, How Can a Hydrophobic MOF be Water-Unstable? Insight into the Hydration Mechanism of IRMOFs, ChemPhysChem, 13 (2012) 3497-3503.
[41] L. Xiong, J. Liu, M. Yu, S. Li, Improving the corrosion protection properties of PVB coating by using salicylaldehyde@ ZIF-8/graphene oxide two-dimensional nanocomposites, Corrosion Science, 146 (2019): 70-79.
[42] Y.J. Tarzanagh, D. Seifzadeh, Z. Rajabalizadeh, A. Habibi-Yangjeh, A. Khodayari, S. Sohrabnezhad, Sol-gel/MOF nanocomposite for effective protection of 2024 aluminum alloy against corrosion, Surface and Coatings Technology, (2019) 125038.
[43] Y. Guo, J. Wang, D. Zhang, T. Qi, G.L. Li, pH-responsive self-healing anticorrosion coatings based on benzotriazole-containing zeolitic imidazole framework, Colloids and Surfaces A: Physicochemical and Engineering Aspects, 561 (2019) 1-8.
[44] Q. Zheng, J. Li, W. Yuan, X. Liu, L. Tan, Y. Zheng, K.W.K. Yeung, S. Wu, Metal–Organic Frameworks Incorporated Polycaprolactone Film for Enhanced Corrosion Resistance and Biocompatibility of Mg Alloy, ACS Sustainable Chemistry & Engineering, 7 (2019) 18114-18124.
[45] M. Ramezanzadeh, B. Ramezanzadeh, M. Mahdavian, G. Bahlakeh, Development of metal-organic framework (MOF) decorated graphene oxide nanoplatforms for anti-corrosion epoxy coatings, Carbon, 161 (2020) 231-251.
[46] N. Wang, Y. Zhang, J. Chen, J. Zhang, Q. Fang, Dopamine modified metal-organic frameworks on anti-corrosion properties of waterborne epoxy coatings, Progress in Organic Coatings, 109 (2017) 126-134.
[47] K. Cao, Z. Yu, D. Yin, Preparation of Ce-MOF@ TEOS to enhance the anti-corrosion properties of epoxy coatings, Progress in Organic Coatings, 135 (2019) 613-621.

[48] B. Ren, Y. Chen, Y. Li, W. Li, S. Gao, H. Li, R. Cao, Rational design of metallic anti-corrosion coatings based on zinc gluconate@ ZIF-8, Chemical Engineering Journal, 384 (2020) 123389.
[49] J. Winarta, B. Shan, S.M. McIntyre, L. Ye, C. Wang, J. Liu, B. Mu, A Decade of UiO-66 Research: A Historic Review of Dynamic Structure, Synthesis Mechanisms, and Characterization Techniques of An Archetypal MOF, Crystal Growth & Design, 20.2 (2019): 1347-1362.
[50] Y. Bai, Y. Dou, L.-H. Xie, W. Rutledge, J.-R. Li, H.-C. Zhou, Zr-based metal–organic frameworks: design, synthesis, structure, and applications, Chemical Society Reviews, 45 (2016) 2327-2367.
[51] F. Ahmadijokani, R. Mohammadkhani, S. Ahmadipouya, A. Shokrgozar, M. Rezakazem, H. Molavi, T.M. Aminabhavi, M. Arjmand, Superior Chemical Stability of UiO-66 metal-organic frameworks (MOFs) for Selective Dye Adsorption, Chemical Engineering Journal, (2020) 125346.
[52] H. He, Q. Sun, W. Gao, J.A. Perman, F. Sun, G. Zhu, B. Aguila, K. Forrest, B. Space, S. Ma, A stable metal–organic framework featuring a local buffer environment for carbon dioxide fixation, Angewandte Chemie, 130 (2018) 4747-4752.
[53] D. Bůžek, J. Demel, K. Lang, Zirconium metal–organic framework UiO-66: stability in an aqueous environment and its relevance for organophosphate degradation, Inorganic chemistry, 57 (2018) 14290-14297.
[54] Y. Peng, R.G. Reddy, Effect of Zr Inhibitor on Corrosion of Haynes 230 and NS-163 Alloys in Flinak, Advances in Molten Slags, Fluxes, and Salts: Proceedings of the 10th International Conference on Molten Slags, Fluxes and Salts 2016, Springer, 2016, pp. 1199-1205.
[55] M. Motamedi, B. Ramezanzadeh, M. Mahdavian, Corrosion inhibition properties of a green hybrid pigment based on Pr-Urtica Dioica plant extract, Journal of Industrial and Engineering Chemistry, 66 (2018) 116-125.
[56] M. Ramezanzadeh, Z. Sanaei, G. Bahlakeh, B. Ramezanzadeh, Highly effective inhibition of mild steel corrosion in 3.5% NaCl solution by green Nettle leaves extract and synergistic effect of eco-friendly cerium nitrate additive: Experimental, MD simulation and QM investigations, Journal of Molecular Liquids, 256 (2018) 67-83.
[57] M. Marinescu, Recent advances in the use of benzimidazoles as corrosion inhibitors, BMC Chemistry, 13 (2019) 136.
[58] M.S. Islam, M. Sakairi, Effects of Zn2+ Concentration on the Corrosion of Mild Steel in NaCl Aqueous Solutions, Journal of The Electrochemical Society, 166 (2019) C83-C90.
[59] W. Guo, S. Nie, E.N. Kalali, X. Wang, W. Wang, W. Cai, L. Song, Y. Hu, Construction of SiO2@ UiO-66 core–shell microarchitectures through covalent linkage as flame retardant and smoke suppressant for epoxy resins, Composites Part B: Engineering, 176 (2019) 107261.
[60] C. Hu, J.-D. Xiao, X.-D. Mao, L.-L. Song, X.-Y. Yang, S.-J. Liu, Toughening mechanisms of epoxy resin using aminated metal-organic framework as additive, Materials Letters, 240 (2019) 113-116.
[61] J. Zhang, Z. Li, L. Zhang, Y. Yang, D.-Y. Wang, Green Synthesis of Biomass Phytic Acid Functionalized UiO-66-NH2 Hierarchical Hybrids Towards Fire safety of Epoxy Resin, ACS Sustainable Chemistry & Engineering, 8.2 (2019): 994-1003.
[62] H.R. Abid, H. Tian, H.-M. Ang, M.O. Tade, C.E. Buckley, S. Wang, Nanosize Zr-metal organic framework (UiO-66) for hydrogen and carbon dioxide storage, Chemical Engineering Journal, 187 (2012) 415-420.

[63] H. Molavi, M. Zamani, M. Aghajanzadeh, H. Kheiri Manjili, H. Danafar, A. Shojaei, Evaluation of UiO-66 metal organic framework as an effective sorbent for Curcumin's overdose, Applied Organometallic Chemistry, 32 (2018) e4221.
[64] H. Molavi, A. Eskandari, A. Shojaei, S.A. Mousavi, Enhancing CO2/N2 adsorption selectivity via post-synthetic modification of NH2-UiO-66 (Zr), Microporous and Mesoporous Materials, 257 (2018) 193-201.
[65] S.D. Accelrys Software Inc., 2009.
[66] A. Klamt, G. Schuurmann, Chem Soc Perkin Trans 2 1993, 5, 799;(b) Baldridge, K.; Klamt, A. J Chem Phys, 106 (1997) 6622.
[67] S.K. Saha, P. Ghosh, A. Hens, N.C. Murmu, P. Banerjee, Density functional theory and molecular dynamics simulation study on corrosion inhibition performance of mild steel by mercapto-quinoline Schiff base corrosion inhibitor, Physica E: Low-dimensional Systems and Nanostructures, 66 (2015) 332-341.
[68] S.K. Saha, M. Murmu, N.C. Murmu, P. Banerjee, Evaluating electronic structure of quinazolinone and pyrimidinone molecules for its corrosion inhibition effectiveness on target specific mild steel in the acidic medium: a combined DFT and MD simulation study, Journal of Molecular Liquids, 224 (2016) 629-638.
[69] L.O. Olasunkanmi, I.B. Obot, M.M. Kabanda, E.E. Ebenso, Some Quinoxalin-6-yl Derivatives as Corrosion Inhibitors for Mild Steel in Hydrochloric Acid: Experimental and Theoretical Studies, J. Phys. Chem. C, 119 (2015) 16004-16019.
[70] C. Verma, L.O. Olasunkanmi, E.E. Ebenso, M.A. Quraishi, I.B. Obot, Adsorption behavior of glucosamine-based, pyrimidine-fused heterocycles as green corrosion inhibitors for mild steel: experimental and theoretical studies, J. Phys. Chem. C, 120 (2016) 11598-11611.
[71] P. Li, Y. Shen, D. Wang, Y. Chen, Y. Zhao, Selective Adsorption-Based Separation of Flue Gas and Natural Gas in Zirconium Metal-Organic Frameworks Nanocrystals, Molecules, 24 (2019) 1822.
[72] P. Yang, Q. Liu, J. Liu, H. Zhang, Z. Li, R. Li, L. Liu, J. Wang, Interfacial growth of a metal–organic framework (UiO-66) on functionalized graphene oxide (GO) as a suitable seawater adsorbent for extraction of uranium (VI), Journal of Materials Chemistry A, 5 (2017) 17933-17942.
[73] L. Valenzano, B. Civalleri, S. Chavan, S. Bordiga, M.H. Nilsen, S. Jakobsen, K.P. Lillerud, C. Lamberti, Disclosing the complex structure of UiO-66 metal organic framework: a synergic combination of experiment and theory, Chemistry of Materials, 23 (2011) 1700-1718.
[74] E.F. López, V.S. Escribano, M. Panizza, M.M. Carnasciali, Vibrational and electronic spectroscopic properties of zirconia powders, Journal of Materials Chemistry, 11 (2001) 1891-1897.
[75] Y. Han, M. Liu, K. Li, Y. Zuo, Y. Wei, S. Xu, G. Zhang, C. Song, Z. Zhang, X. Guo, Facile synthesis of morphology and size-controlled zirconium metal–organic framework UiO-66: the role of hydrofluoric acid in crystallization, CrystEngComm, 17 (2015) 6434-6440.
[76] F. Ragon, B. Campo, Q. Yang, C. Martineau, A.D. Wiersum, A. Lago, V. Guillerm, C. Hemsley, J.F. Eubank, M. Vishnuvarthan, Acid-functionalized UiO-66 (Zr) MOFs and their evolution after intra-framework cross-linking: structural features and sorption properties, Journal of Materials Chemistry A, 3 (2015) 3294-3309.
[77] J.H. Cavka, S. Jakobsen, U. Olsbye, N. Guillou, C. Lamberti, S. Bordiga, K.P. Lillerud, A new zirconium inorganic building brick forming metal organic frameworks with exceptional stability, Journal of the American Chemical Society, 130 (2008) 13850-13851.

[78] Z. Jin, H. Yang, Exploration of Zr–metal–organic framework as efficient photocatalyst for hydrogen production, Nanoscale research letters, 12 (2017) 539.
[79] W. Xu, M. Dong, L. Di, X. Zhang, A Facile Method for Preparing UiO-66 Encapsulated Ru Catalyst and its Application in Plasma-Assisted CO2 Methanation, Nanomaterials, 9 (2019) 1432.
[80] M.A. Rodrigues, J. de Souza Ribeiro, E. de Souza Costa, J.L. de Miranda, H.C. Ferraz, Nanostructured membranes containing UiO-66 (Zr) and MIL-101 (Cr) for O2/N2 and CO2/N2 separation, Separation and Purification Technology, 192 (2018) 491-500.
[81] G.Y. Shangkum, P. Chammingkwan, D.X. Trinh, T. Taniike, Design of a semi-continuous selective layer based on deposition of UiO-66 nanoparticles for nanofiltration, Membranes, 8 (2018) 129.
[82] H. Molavi, M. Neshastehgar, A. Shojaei, H. Ghashghaeinejad, Ultrafast and simultaneous removal of anionic and cationic dyes by nanodiamond/UiO-66 hybrid nanocomposite, Chemosphere, (2020) 125882.
[83] X. Zhang, Y. Zhang, T. Wang, Z. Fan, G. Zhang, A thin film nanocomposite membrane with pre-immobilized UiO-66-NH 2 toward enhanced nanofiltration performance, RSC advances, 9 (2019) 24802-24810.
[84] A.X. Lu, M. McEntee, M.A. Browe, M.G. Hall, J.B. DeCoste, G.W. Peterson, MOFabric: Electrospun nanofiber mats from PVDF/UiO-66-NH2 for chemical protection and decontamination, ACS applied materials & interfaces, 9 (2017) 13632-13636.
[85] L. Shen, S. Liang, W. Wu, R. Liang, L. Wu, Multifunctional NH 2-mediated zirconium metal–organic framework as an efficient visible-light-driven photocatalyst for selective oxidation of alcohols and reduction of aqueous Cr (vi), Dalton Transactions, 42 (2013) 13649-13657.
[86] H. Molavi, F.A. Joukani, A. Shojaei, Ethylenediamine grafting to functionalized NH2–UiO-66 using green aza-michael addition reaction to improve CO2/CH4 adsorption selectivity, Industrial & Engineering Chemistry Research, 57 (2018) 7030-7039.
[87] R. Wu, X. Qian, K. Zhou, H. Liu, B. Yadian, J. Wei, H. Zhu, Y. Huang, Highly dispersed Au nanoparticles immobilized on Zr-based metal–organic frameworks as heterostructured catalyst for CO oxidation, Journal of Materials Chemistry A, 1 (2013) 14294-14299.
[88] J. Zhang, T. Xia, D. Zhao, Y. Cui, Y. Yang, G. Qian, In situ secondary growth of Eu (III)-organic framework film for fluorescence sensing of sulfur dioxide, Sensors and Actuators B: Chemical, 260 (2018) 63-69.
[89] B. Mirhosseini-Eshkevari, M.A. Ghasemzadeh, M. Esnaashari, S.T. Ganjali, Introduction of a Novel Brønsted Acidic Ionic Liquid Incorporated in UiO-66 Nanocages for the Efficient Synthesis of Pyrimido [4, 5-d] Pyrimidines, ChemistrySelect, 4 (2019) 12920-12927.
[90] J. Zhu, L. Wu, Z. Bu, S. Jie, B.-G. Li, Polyethyleneimine-Modified UiO-66-NH2 (Zr) Metal–Organic Frameworks: Preparation and Enhanced CO2 Selective Adsorption, ACS omega, 4 (2019) 3188-3197.
[91] M. Kandiah, M.H. Nilsen, S. Usseglio, S. Jakobsen, U. Olsbye, M. Tilset, C. Larabi, E.A. Quadrelli, F. Bonino, K.P. Lillerud, Synthesis and stability of tagged UiO-66 Zr-MOFs, Chemistry of Materials, 22 (2010) 6632-6640.
[92] Q. Chen, Q. He, M. Lv, Y. Xu, H. Yang, X. Liu, F. Wei, Selective adsorption of cationic dyes by UiO-66-NH2, Applied Surface Science, 327 (2015) 77-85.
[93] M. Aghajanzadeh, M. Zamani, H. Molavi, H.K. Manjili, H. Danafar, A. Shojaei, Preparation of metal–organic frameworks UiO-66 for adsorptive removal of methotrexate from aqueous solution, Journal of Inorganic and Organometallic Polymers and Materials, 28 (2018) 177-186.

[94] J.B. DeCoste, G.W. Peterson, H. Jasuja, T.G. Glover, Y.-g. Huang, K.S. Walton, Stability and degradation mechanisms of metal–organic frameworks containing the Zr 6 O 4 (OH) 4 secondary building unit, Journal of Materials Chemistry A, 1 (2013) 5642-5650.
[95] Z.-S. Qin, W.-W. Dong, J. Zhao, Y.-P. Wu, Q. Zhang, D.-S. Li, A water-stable Tb (III)-based metal–organic gel (MOG) for detection of antibiotics and explosives, Inorganic Chemistry Frontiers, 5 (2018) 120-126.
[96] A.A. Javidparvar, R. Naderi, B. Ramezanzadeh, Designing a potent anti-corrosion system based on graphene oxide nanosheets non-covalently modified with cerium/benzimidazole for selective delivery of corrosion inhibitors on steel in NaCl media, Journal of Molecular Liquids, 284 (2019): 415-430.
[97] R. Samiee, B. Ramezanzadeh, M. Mahdavian, E. Alibakhshi, Assessment of the smart self-healing corrosion protection properties of a water-base hybrid organo-silane film combined with non-toxic organic/inorganic environmentally friendly corrosion inhibitors on mild steel, Journal of Cleaner Production, 220 (2019) 340-356.
[98] S. Zheng, D.A. Bellido-Aguilar, J. Hu, Y. Huang, X. Zhao, Z. Wang, X. Zeng, Q. Zhang, Z. Chen, Waterborne bio-based epoxy coatings for the corrosion protection of metallic substrates, Progress in Organic Coatings, 136 (2019) 105265.
[99] A.A. Javidparvar, R. Naderi, B. Ramezanzadeh, Epoxy-polyamide nanocomposite coating with graphene oxide as cerium nanocontainer generating effective dual active/barrier corrosion protection, Composites Part B: Engineering, 172 (2019) 363-375.
[100] A. Habibiyan, B. Ramezanzadeh, M. Mahdavian, G. Bahlakeh, M. Kasaeian, Rational Assembly of Mussel-Inspired Polydopamine (PDA)-Zn (II) Complex Nanospheres on Graphene Oxide Framework Tailored for Robust Self-Healing Anti-Corrosion Coatings Application, Chemical Engineering Journal, (2019) 123630.
[101] F. Mansfeld, C. Tsai, Determination of coating deterioration with EIS: I. Basic relationships, Corrosion, 47 (1991) 958-963.
[102] B. Ramezanzadeh, S. Niroumandrad, A. Ahmadi, M. Mahdavian, M.M. Moghadam, Enhancement of barrier and corrosion protection performance of an epoxy coating through wet transfer of amino functionalized graphene oxide, Corrosion Science, 103 (2016) 283-304.
[103] A. Xu, F. Zhang, F. Jin, R. Zhang, B. Luo, T. Zhang, The evaluation of coating performance by analyzing the intersection of bode plots, Int. J. Electrochem. Sci, 9 (2014) 5116-5125.
[104] X. Wang, F. Tang, X. Qi, Z. Lin, D. Battocchi, X. Chen, Enhanced Protective Coatings Based on Nanoparticle fullerene C60 for Oil & Gas Pipeline Corrosion Mitigation, Nanomaterials, 9 (2019) 1476.
[105] P.A. Sørensen, S. Kiil, K. Dam-Johansen, C.E. Weinell, Anticorrosive coatings: a review, Journal of Coatings Technology and Research, 6 (2009) 135-176.
[106] B. Ramezanzadeh, A. Ahmadi, M. Mahdavian, Enhancement of the corrosion protection performance and cathodic delamination resistance of epoxy coating through treatment of steel substrate by a novel nanometric sol-gel based silane composite film filled with functionalized graphene oxide nanosheets, Corrosion Science, 109 (2016) 182-205.
[107] J. McHattie, I. Perez, J. Kehr, Factors affecting cathodic disbondment of epoxy coatings for steel reinforcing bars, Cement and Concrete Composites, 18 (1996) 93-103.
[108] M. Harun, J. Marsh, S. Lyon, The effect of surface modification on the cathodic disbondment rate of epoxy and alkyd coatings, Progress in organic coatings, 54 (2005) 317-321.
[109] B. Ramezanzadeh, Z. Haeri, M. Ramezanzadeh, A facile route of making silica nanoparticles-covered graphene oxide nanohybrids (SiO2-GO); fabrication of SiO2-GO/epoxy

composite coating with superior barrier and corrosion protection performance, Chemical Engineering Journal, 303 (2016) 511-528.
[110] M.T. Majd, M. Davoudi, M. Ramezanzadeh, E. Ghasemi, B. Ramezanzadeh, M. Mahdavian, Construction of a smart active/barrier anti-corrosion system based on epoxy-ester/zinc intercalated kaolin nanocontainer for steel substrate, Construction and Building Materials, 247 (2020) 118555.
[111] S. Zheng, D.A. Bellido-Aguilar, Y. Huang, X. Zeng, Q. Zhang, Z. Chen, Mechanically robust hydrophobic bio-based epoxy coatings for anti-corrosion application, Surface and Coatings Technology, 363 (2019) 43-50.
[112] D.A. Bellido-Aguilar, S. Zheng, X. Zhan, Y. Huang, X. Zhao, X. Zeng, P.K. Pallathadka, Q. Zhang, Z. Chen, Effect of a fluoroalkyl-functional curing agent on the wettability, thermal and mechanical properties of hydrophobic biobased epoxy coatings, Surface and Coatings Technology, 362 (2019) 274-281.
[113] M. Ramezanzadeh, G. Bahlakeh, Z. Sanaei, B. Ramezanzadeh, Corrosion inhibition of mild steel in 1 M HCl solution by ethanolic extract of eco-friendly Mangifera indica (mango) leaves: Electrochemical, molecular dynamics, Monte Carlo and ab initio study, Applied Surface Science, 463 (2019) 1058-1077.
[114] A.Y. Musa, R.T. Jalgham, A.B. Mohamad, Molecular dynamic and quantum chemical calculations for phthalazine derivatives as corrosion inhibitors of mild steel in 1M HCl, Corrosion Science, 56 (2012) 176-183.
[115] K. Khaled, Studies of iron corrosion inhibition using chemical, electrochemical and computer simulation techniques, Electrochimica Acta, 55 (2010) 6523-6532.
[116] J. Zhang, G. Qiao, S. Hu, Y. Yan, Z. Ren, L. Yu, Theoretical evaluation of corrosion inhibition performance of imidazoline compounds with different hydrophilic groups, Corrosion Science, 53 (2011) 147-152.

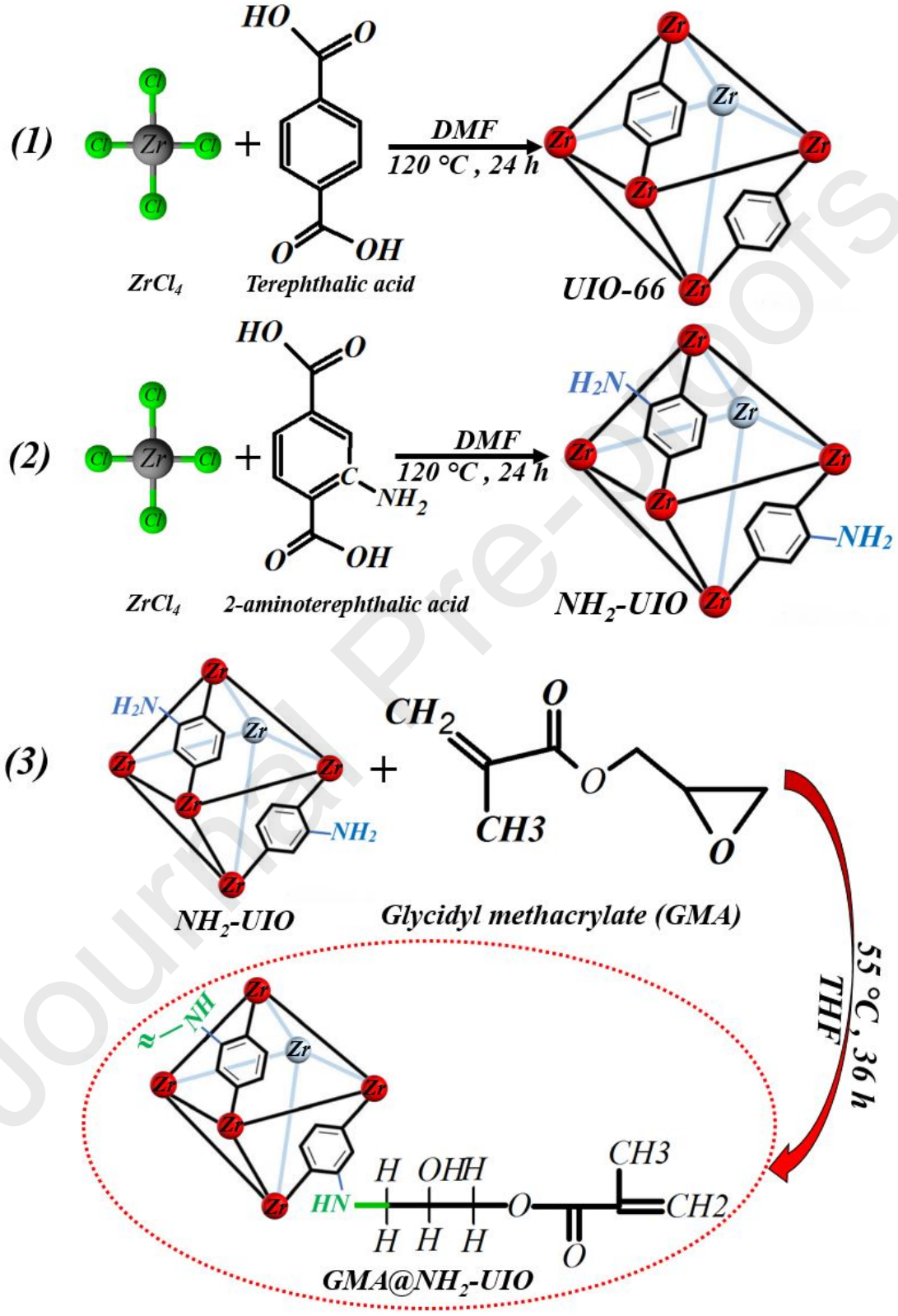

Figure 1. Synthesis of UIO-66 and NH_2-UIO and GMA@NH_2-UIO particles.

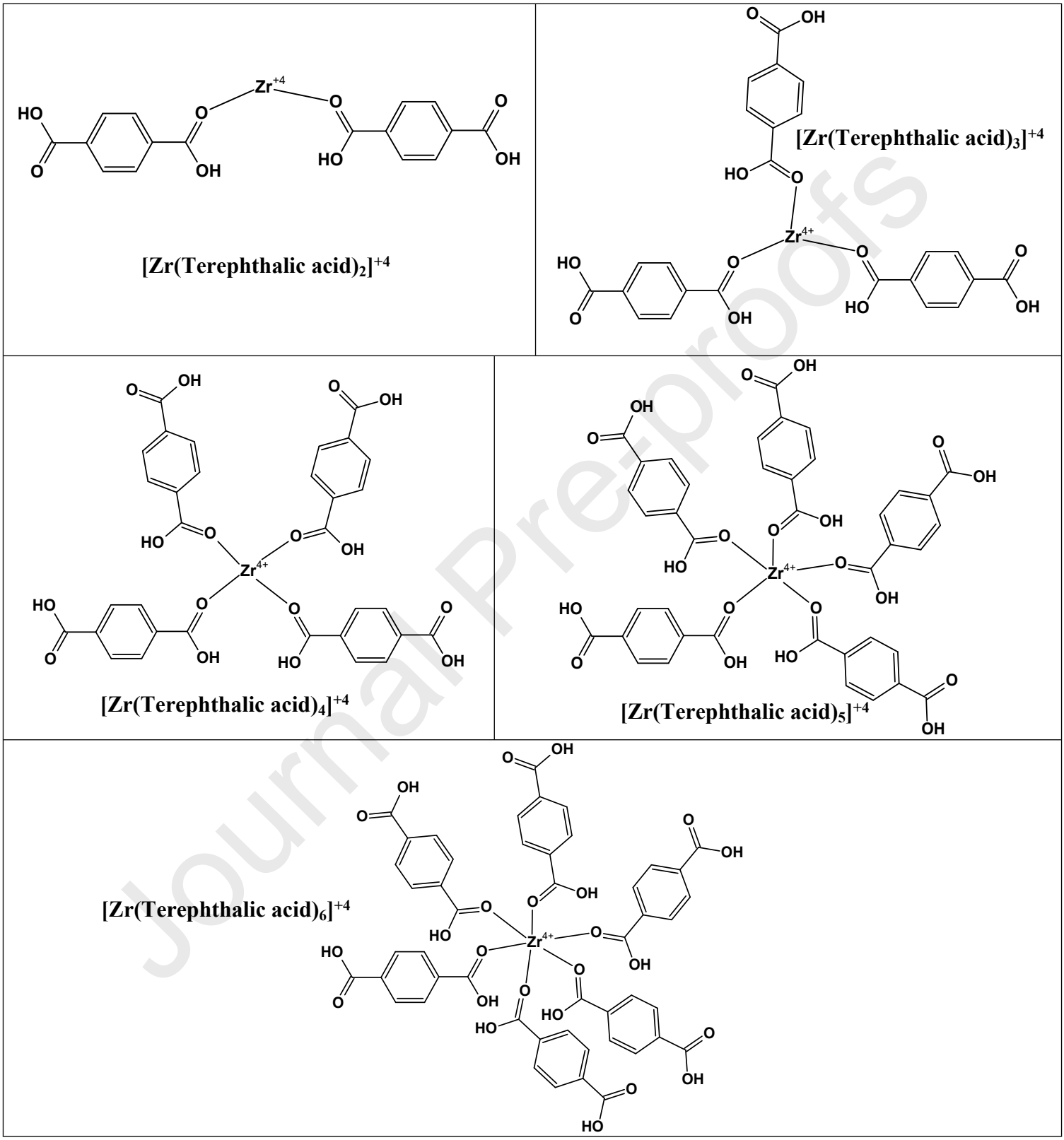

Figure 2. The designed complexes between zirconium (IV) cation and terephthalic acid.

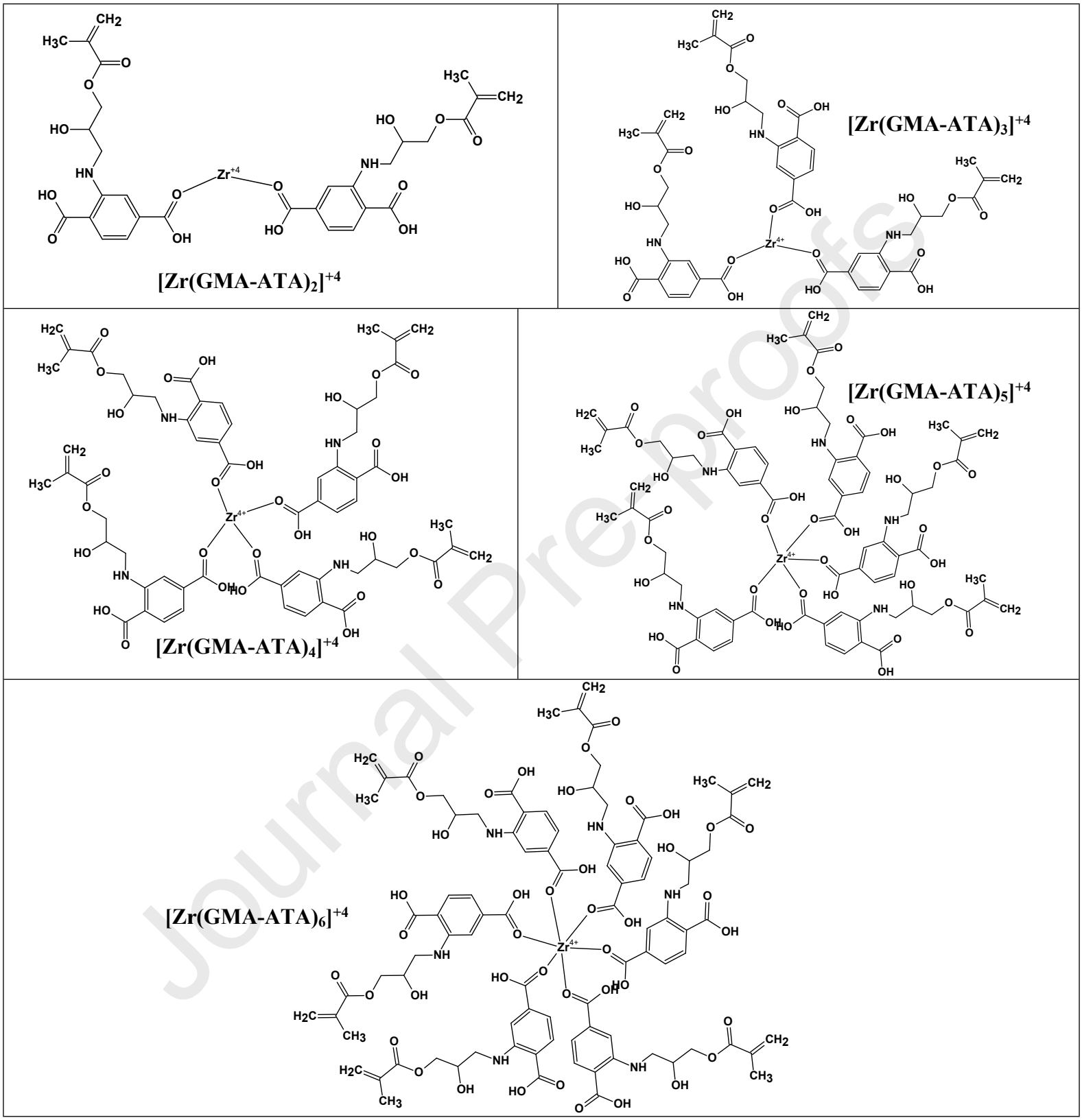

Figure 3. The designed complexes between zirconium (IV) cation and glycidyl methacrylate (GMA) functionalized 2-aminoterephthalic acid.

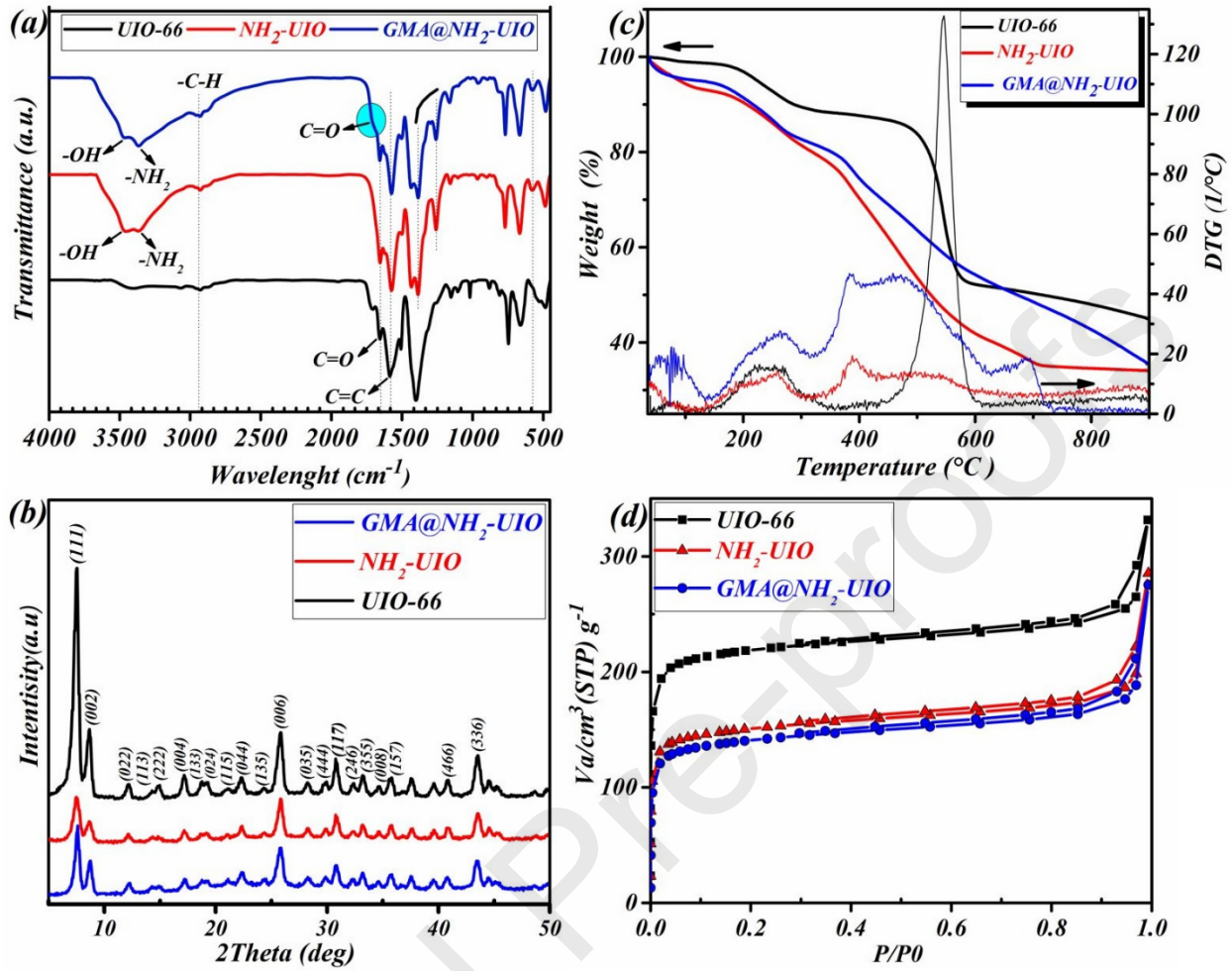

Figure 4. FT-IR spectra (a), XRD patterns (b), TGA diagrams (c), and (d) BET plots for UIO-66, NH_2.UIO, and GMA@NH_2.UIO samples, respectively.

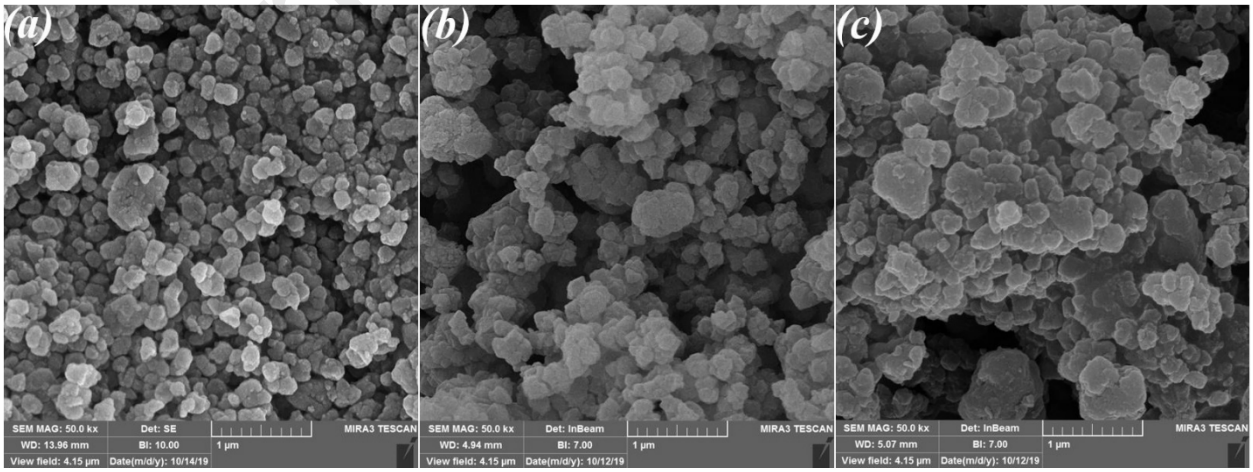

Figure 5. FE-SEM images related to the UIO-66 (a), NH_2-UIO (b) and GMA@NH_2-UIO (c) particles respectively.

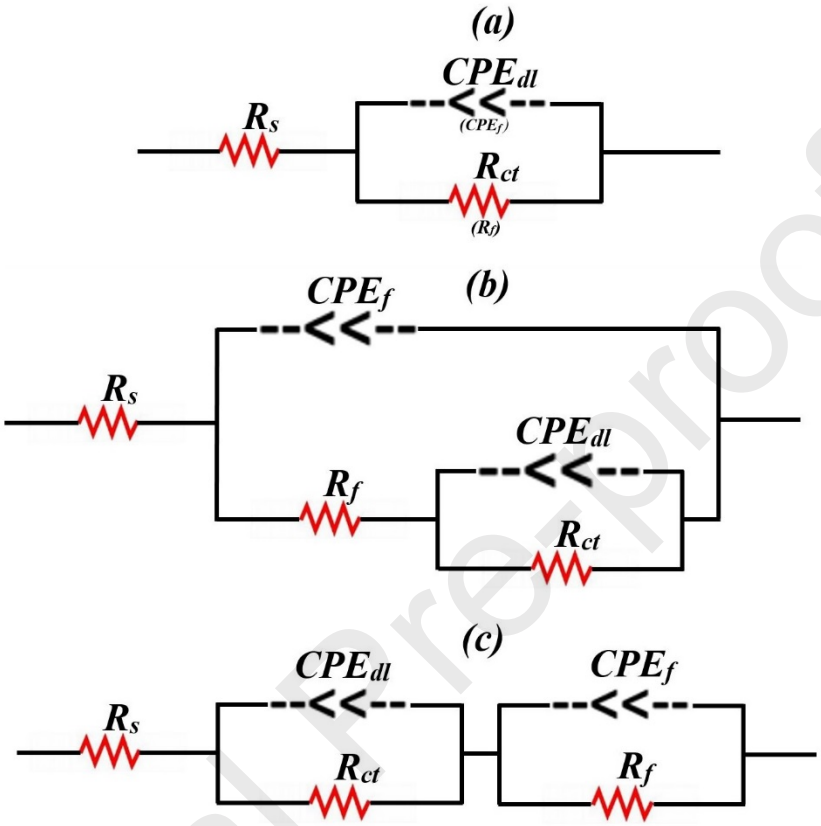

Figure 6. The one-time constant (a) and two times constant EEC models in the parallel (b) and series (c) states used for impedance results simulation.

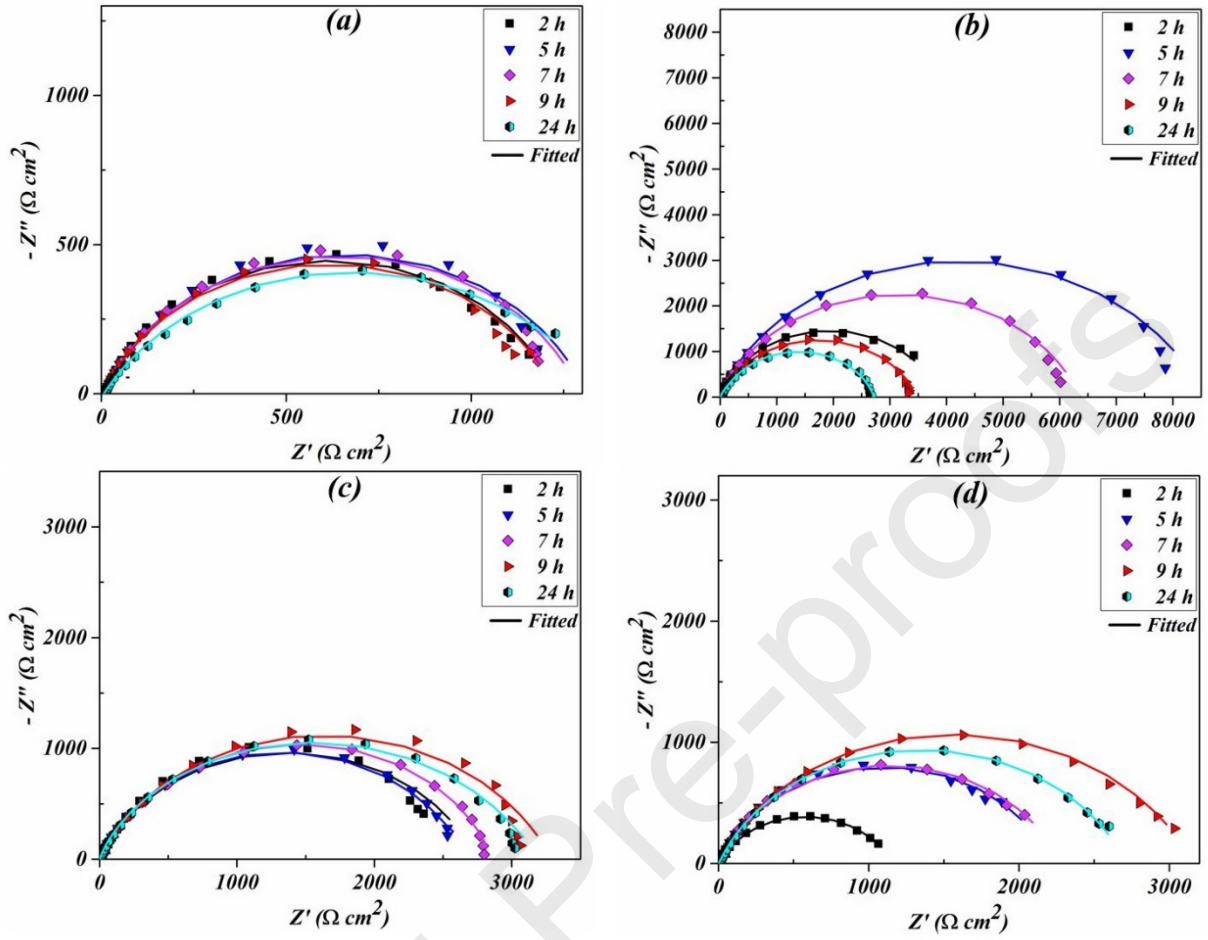

Figure 7. Nyquist plots for bare steel panels (1 cm × 1 cm) exposed in 3.5 wt. % chloride, (a) saline, (b) UIO, (c) NH_2-UIO and (d) GMA@NH_2-UIO extract solutions (for 48 h extraction time) at different exposed times.

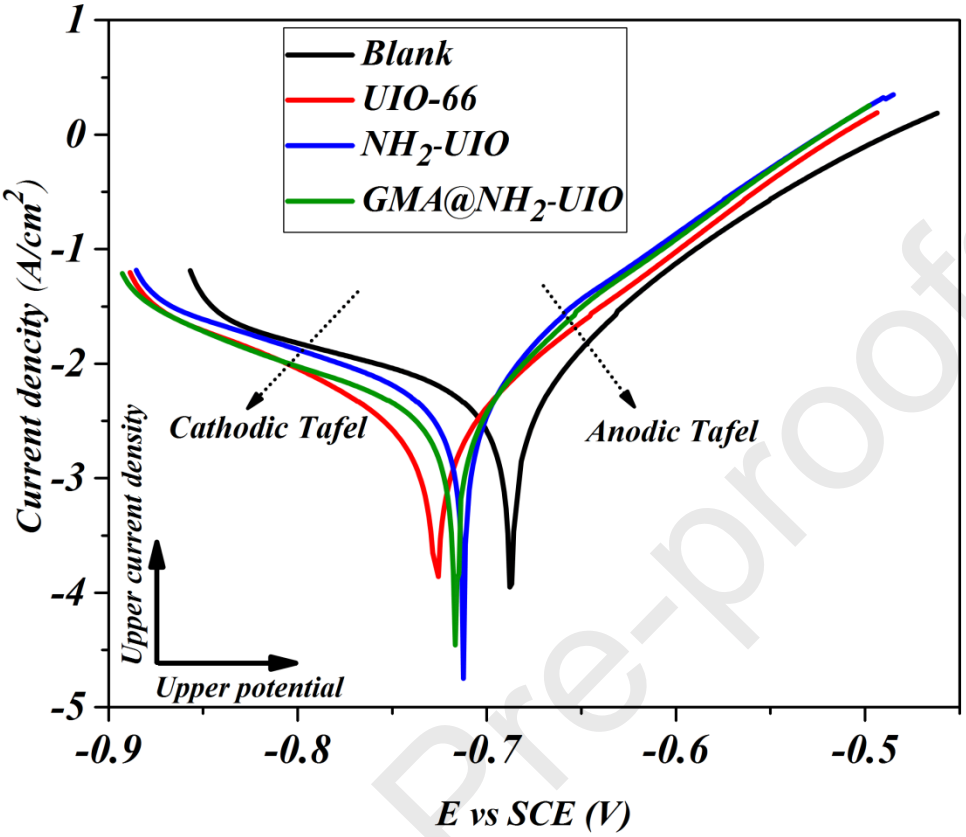

Figure 8. Polarization plots for the mild steel panels (1 cm × 1 cm) exposed in the in 3.5 wt. % chloride saline (Blank), UIO-66, NH_2-UIO and GMA@NH_2-UIO extract solutions (48 h extract time) after 9 h immersion time.

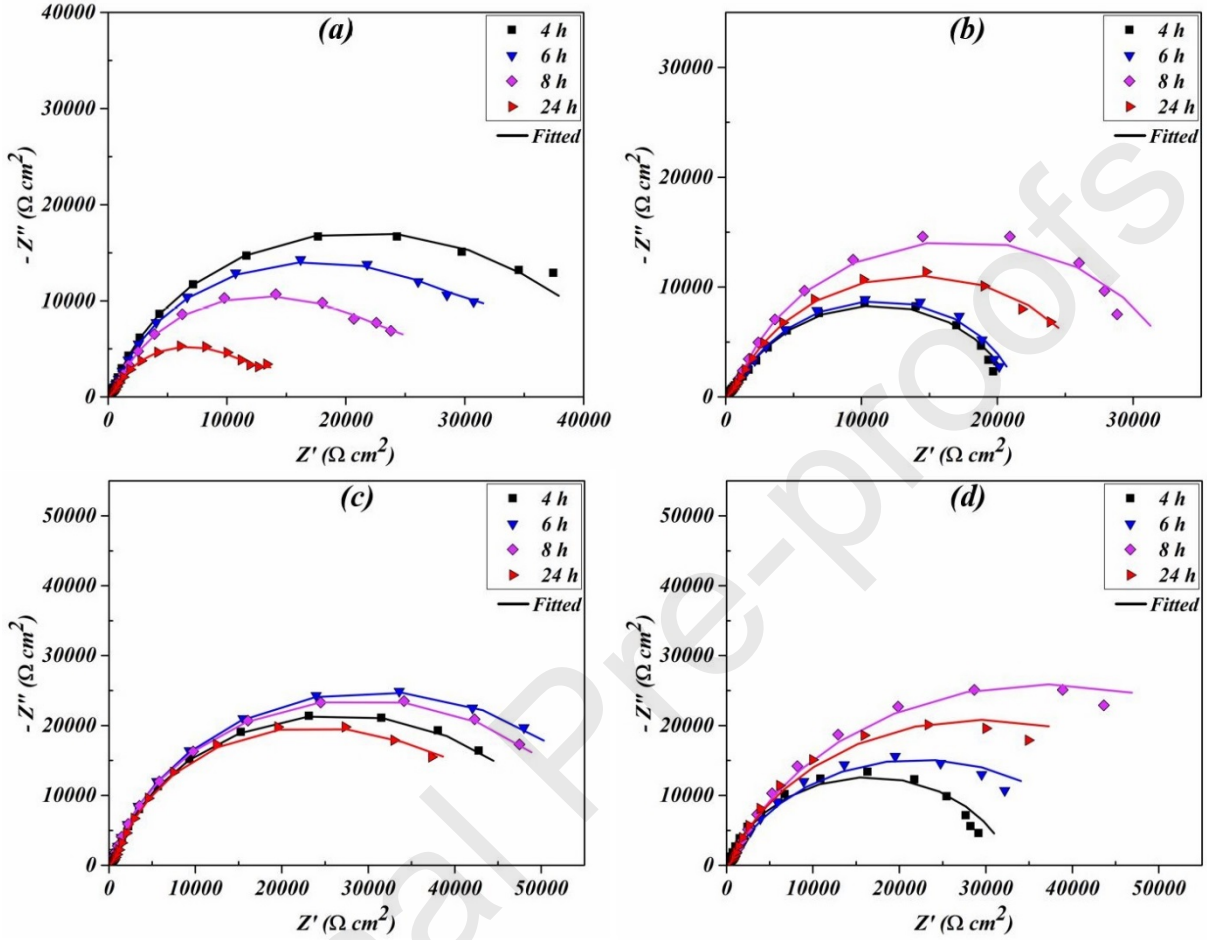

Figure 9. Nyquist plots of the (a): EP, (b): UIO/EP, (c): UIN/EP and (d): G-UIN/EP samples (2 cm × 2 cm) with an artificial defect (1 cm in length) immersed in 3.5 wt. % chloride solution for different immersion times.

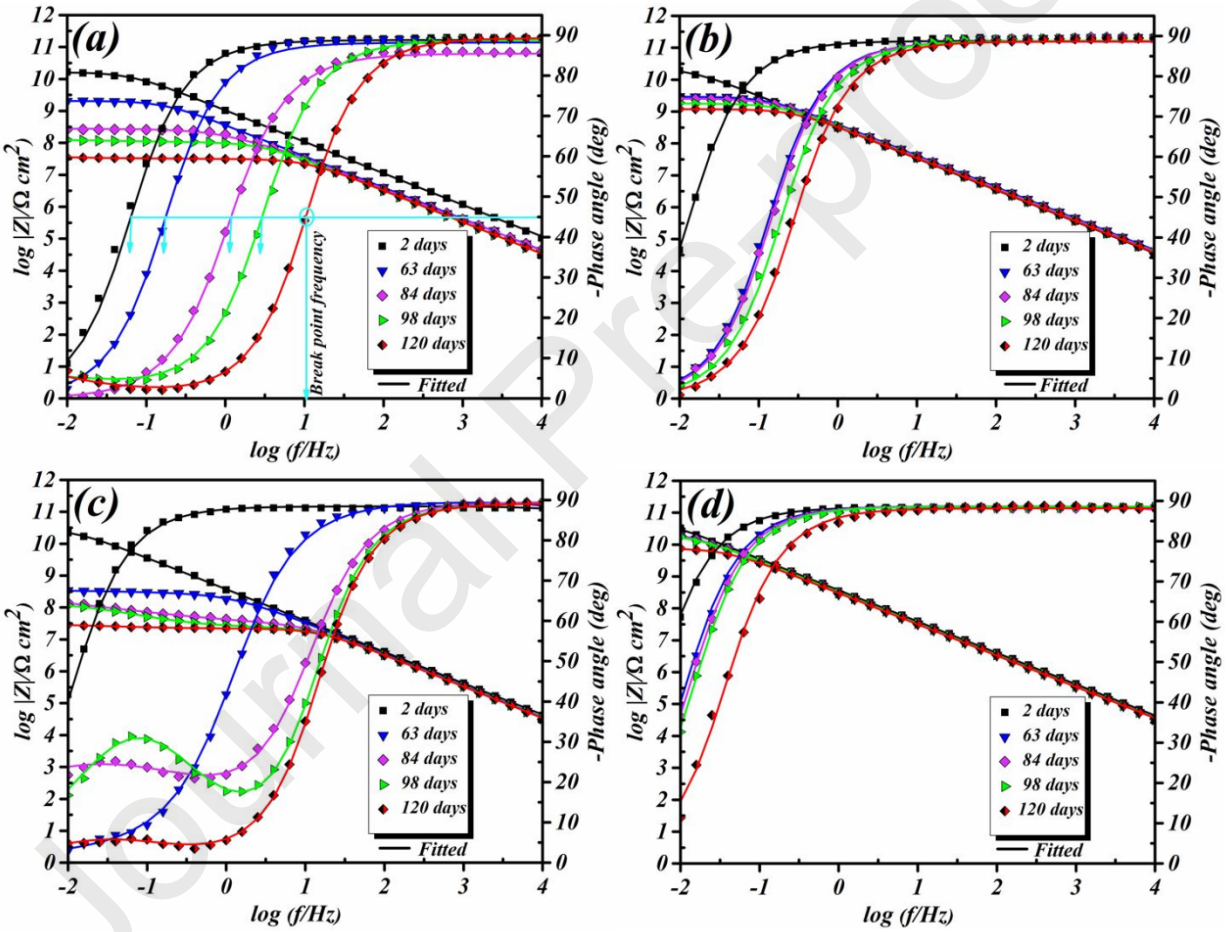

Figure 10. Bode plots of the (a): EP, (b): UIO/EP, (c): UIN/EP and (d): G-UIN/EP samples (2 cm × 2 cm) immersed in 3.5 wt. % chloride solution for different times.

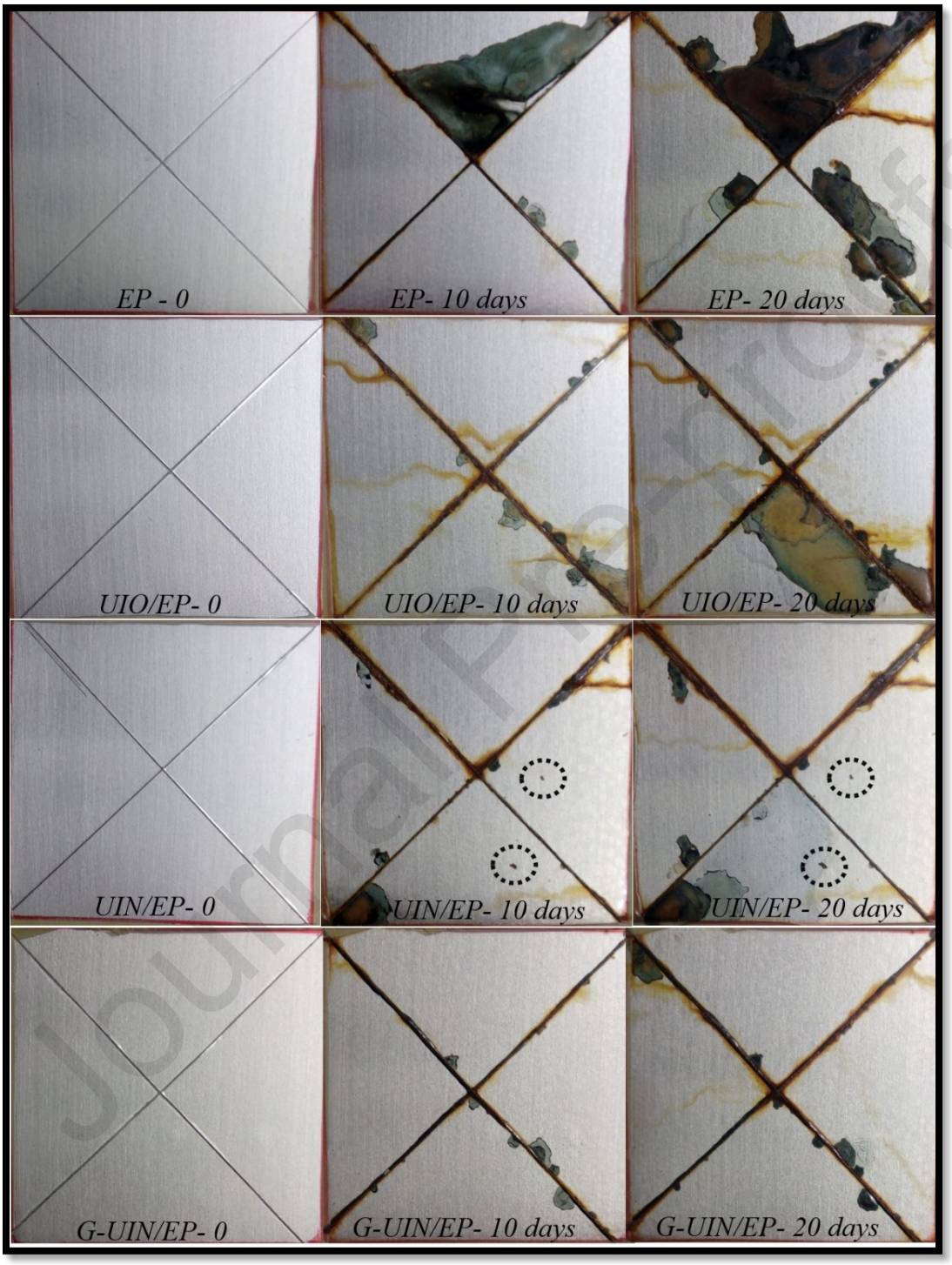

Figure 11. Salt spay test (0, 10 and 20 days) result for the EP, UIO/Epoxy, UIN/Epoxy, and G-UIN/EP samples.

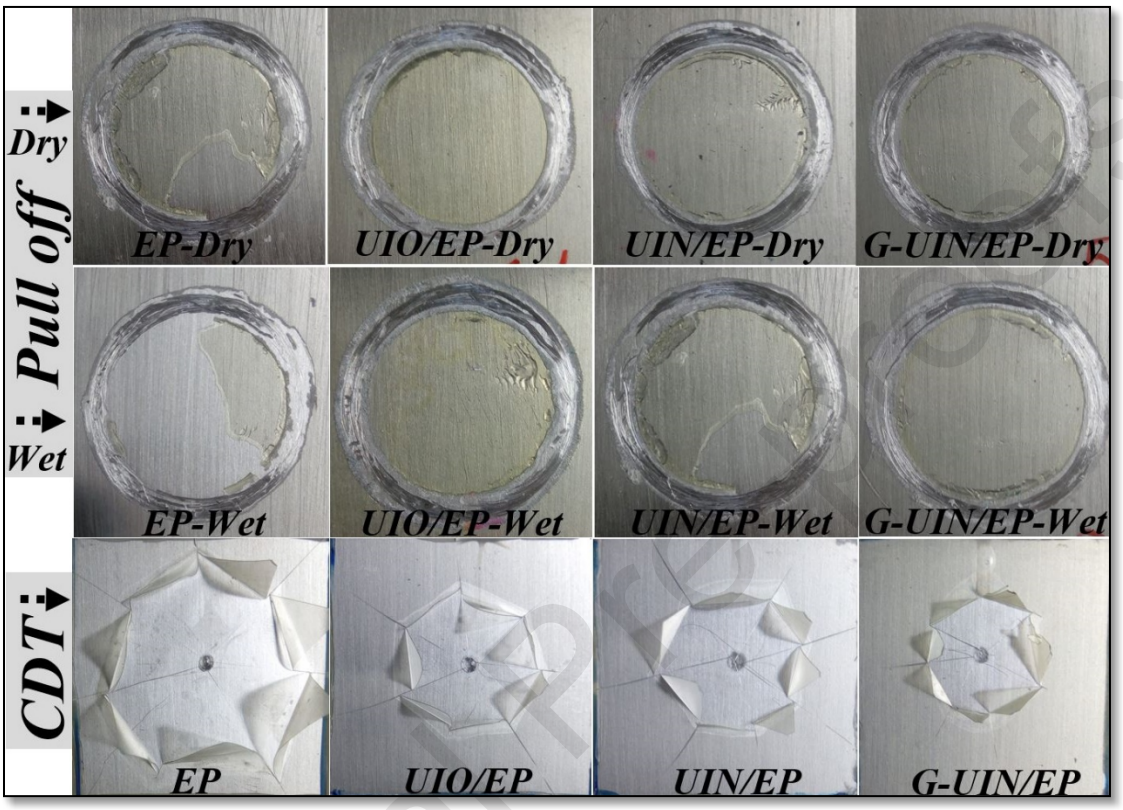

Figure 12. Pull off (dry and wet) and chathodic disbonding (-2 V vs SCE, 25 °C,1 day) results for the EP, UIO/EP, UIN/EP, and G-UIN/EP samples.

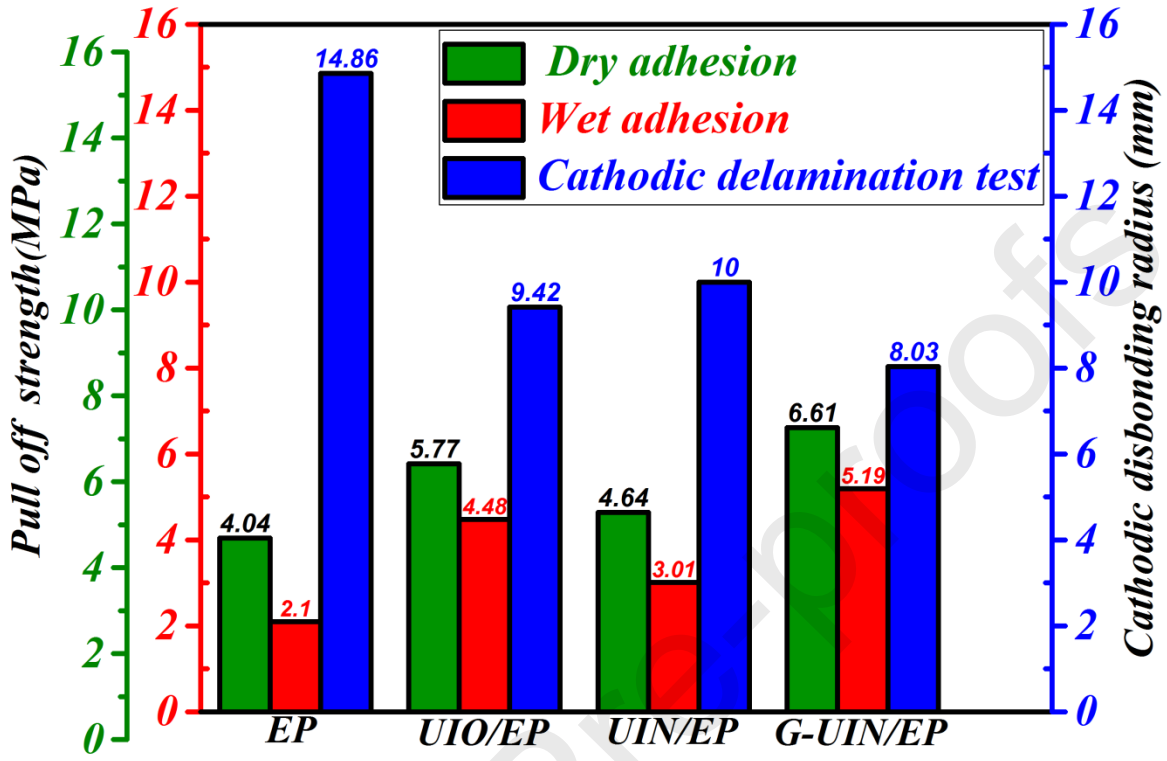

Figure 13. Pull-off (dry and wet(after 14 days SST)) and cathodic disbonding (-2 V vs SCE, 25 °C, 1 day) results for EP, UIO/EP, UIN/EPand G-UIN/EP.

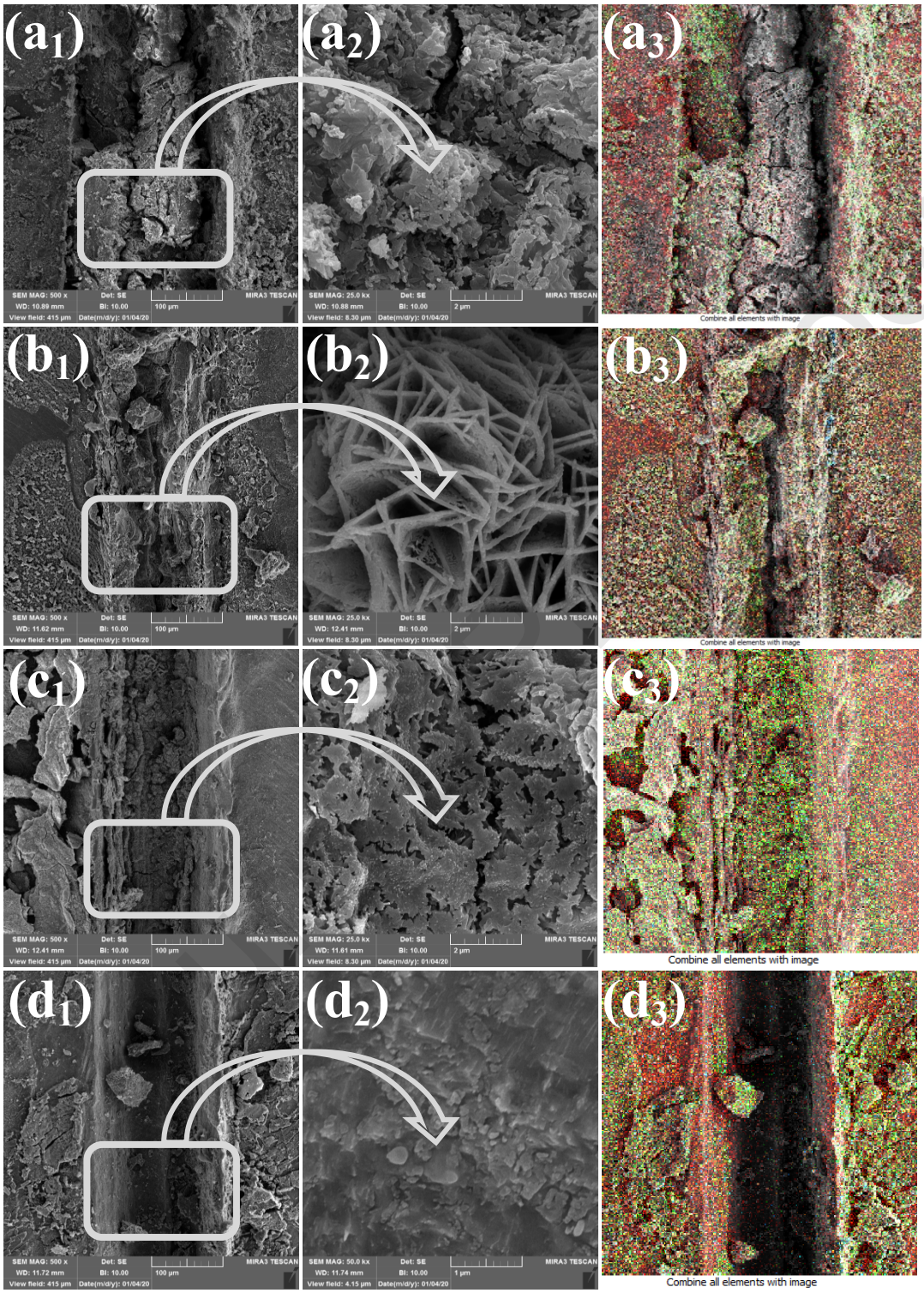
(a1)
(a2)
(a3)
Combine all elements with image
(b1)
(b2)
(b3)
Combine all elements with image
(c1)
(c2)
(c3)
Combine all elements with image
(d1)
(d2)
(d3)
Combine all elements with image

Figure 14. FE-SEM micrographs and corresponding map analysis of (a_1,a_2) and (a_3): EP, (b_1,b_2) and (b_3): UIO/EP, (c_1,c_2) and (c_3): UIN/EP and (d_1,d_2) and (d_3): G-UIN/EP samples with an artificial defect immersed in the salty solution respectively. (Red:Fe, Blue:C, Green: O, Cyan blue: N, Gray: Zr).

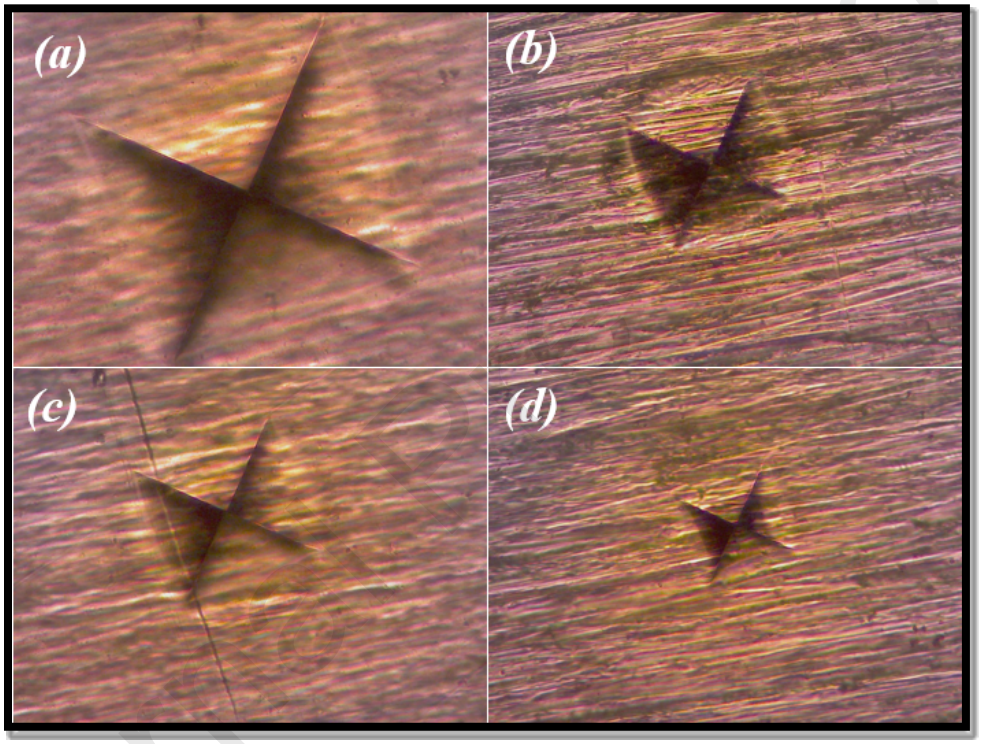

Figure 15. Optical microscopic images of the Vickers indent morphology for (a) EP, (b) UIO/EP, (C) UIN/EP, and (d) G-UIN/EP samples after Vickers micro-hardness test with a load of 0.1 kg at an indentation time of 10 seconds.

	$[Zr(TA)_n]^{+4}$	$[Zr(ATA)_n]^{+4}$	$[Zr(GMA\text{-}ATA)_n]^{+4}$
n=2	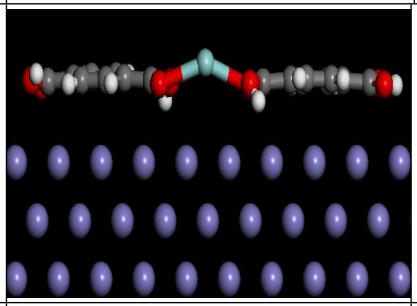	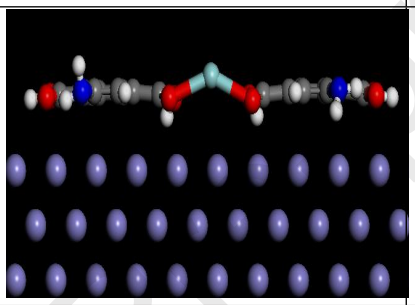	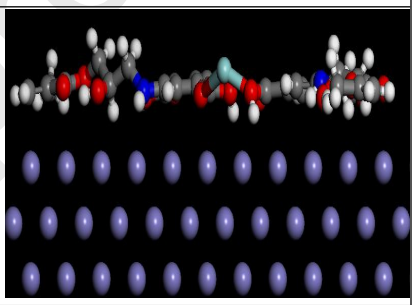
n=3	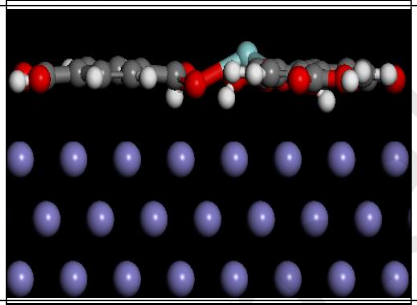	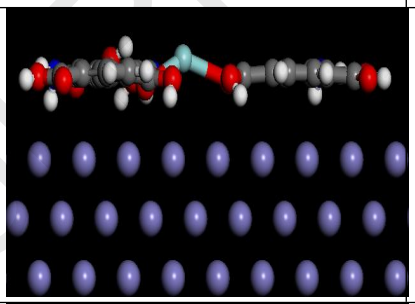	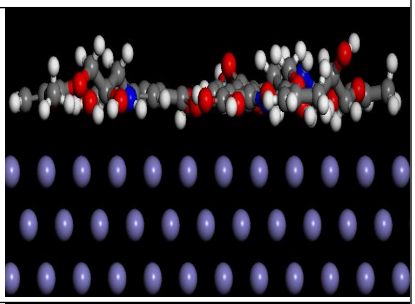
n=4	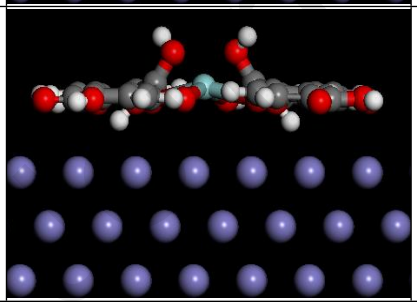	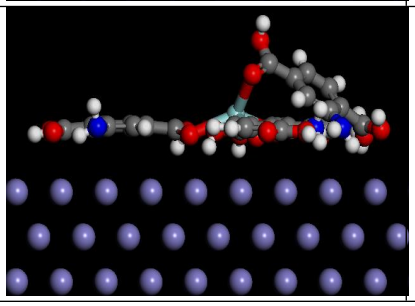	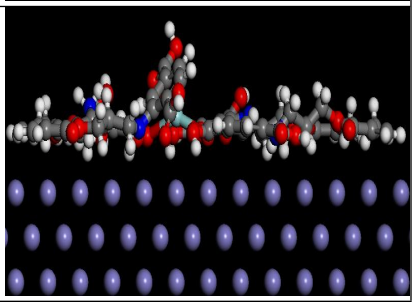

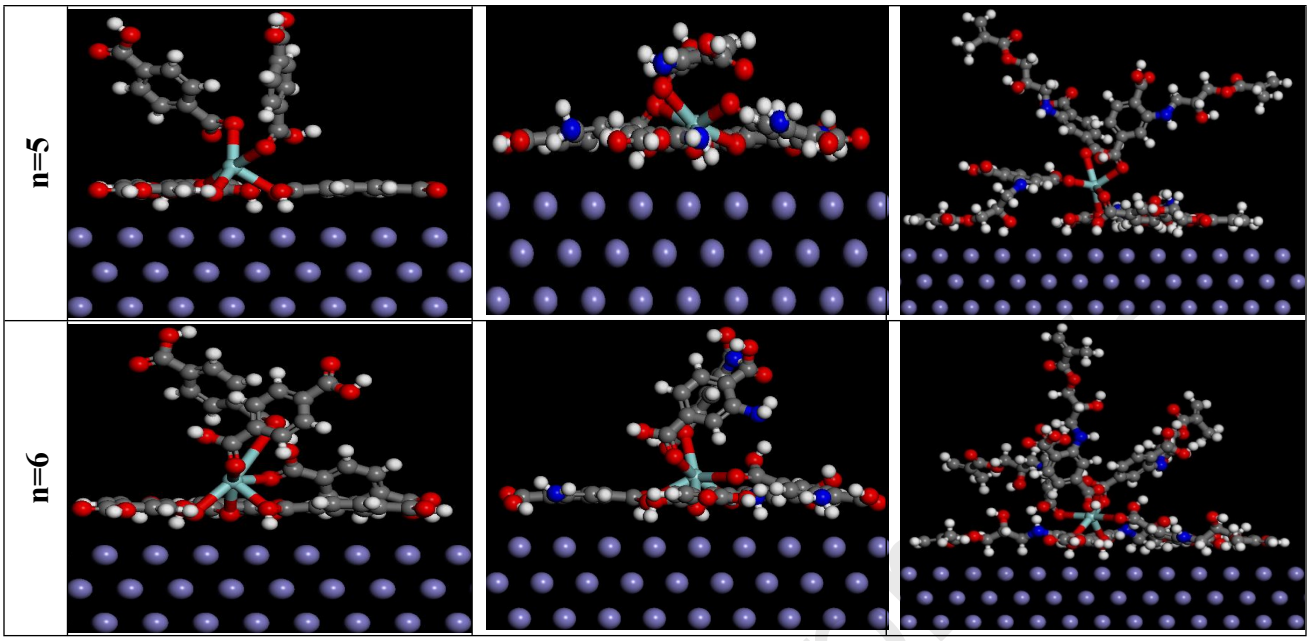

Figure 16. MC simulated snapshots of zirconium (IV) (Zr^{+4}) complexes with terephthalic acid (TA) $[Zr(TA)_n]^{+4}$, 2-aminoterephthalic acid (ATA) $[Zr(ATA)_n]^{+4}$, and glycidyl methacrylate (GMA) functionalized 2-aminoterephthalic acid (GMA-ATA) $[Zr(GMA\text{-}ATA)_n]^{+4}$.

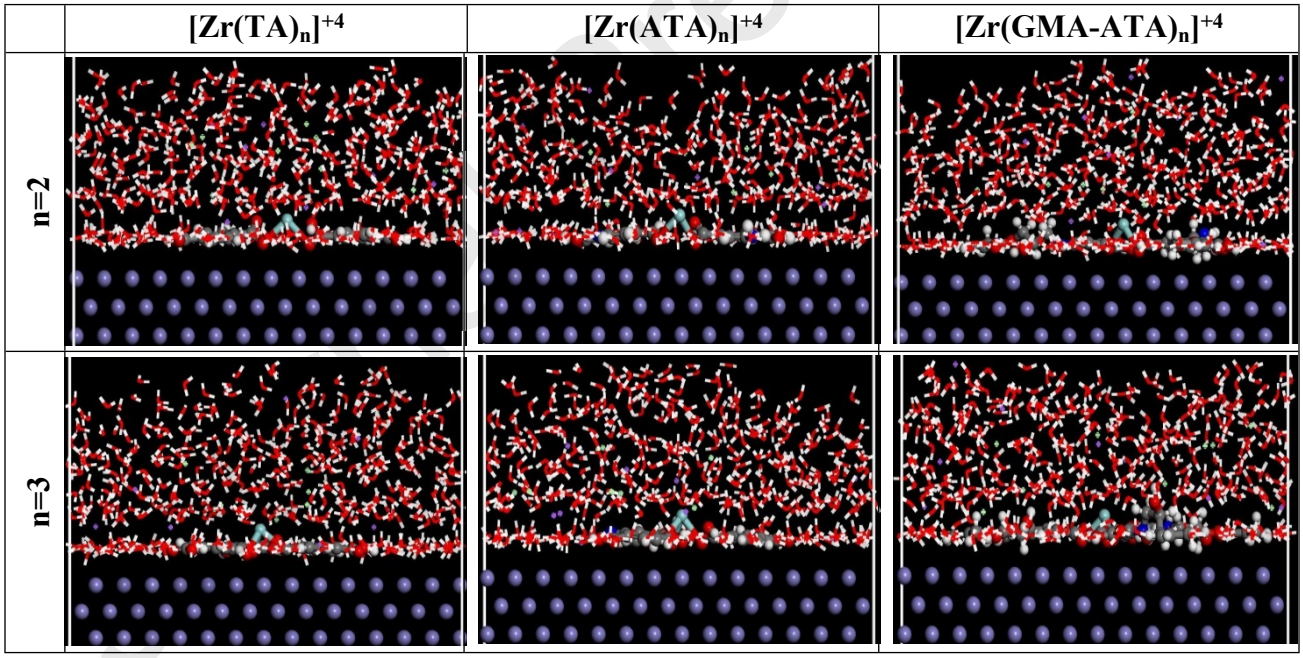

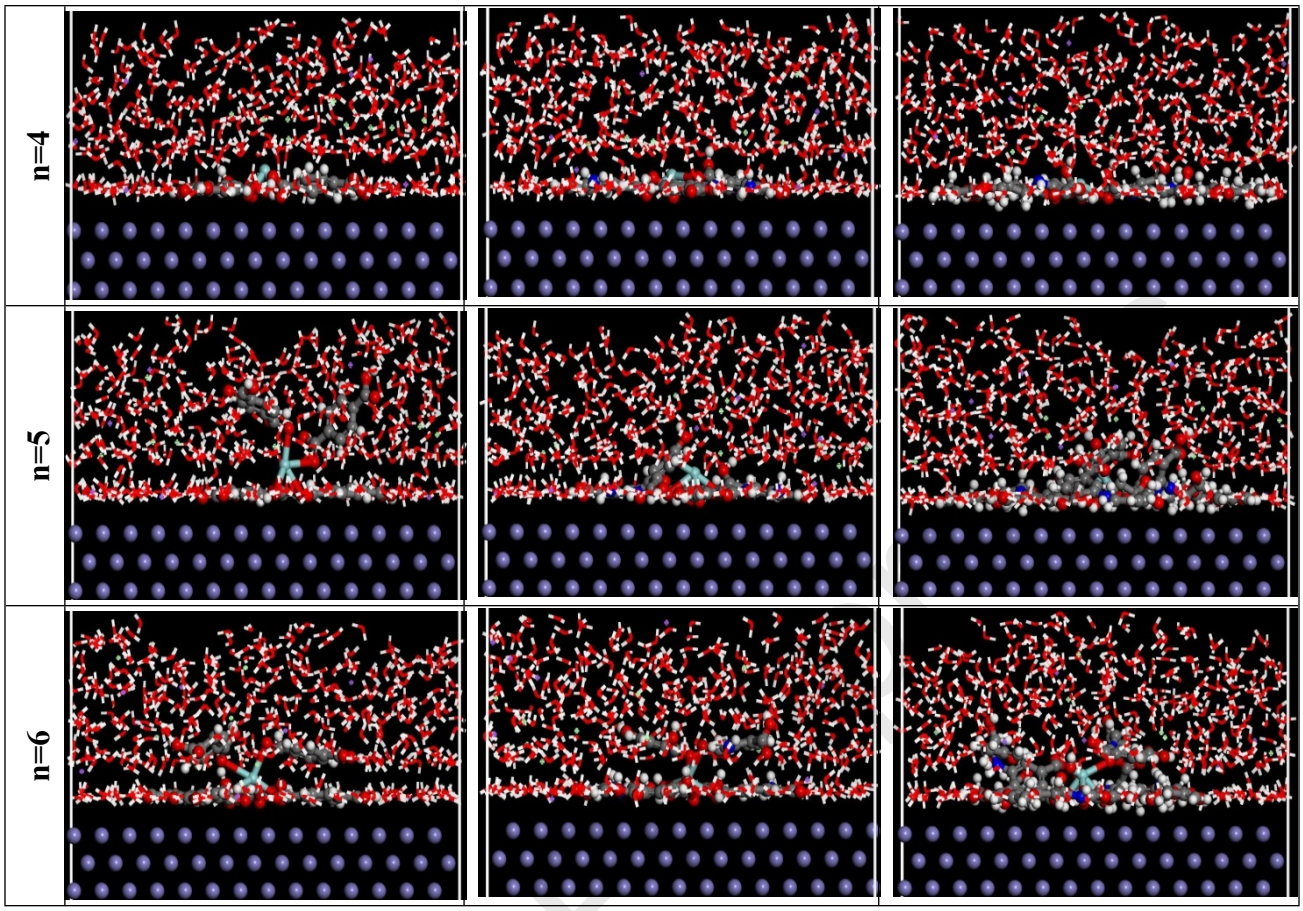

Figure 17. MD simulated snapshots of zirconium (IV) (Zr^{+4}) complexes with terephthalic acid (TA) $[Zr(TA)_n]^{+4}$, 2-aminoterephthalic acid (ATA) $[Zr(ATA)_n]^{+4}$, and glycidyl methacrylate (GMA) functionalized 2-aminoterephthalic acid (GMA-ATA) $[Zr(GMA\text{-}ATA)_n]^{+4}$.

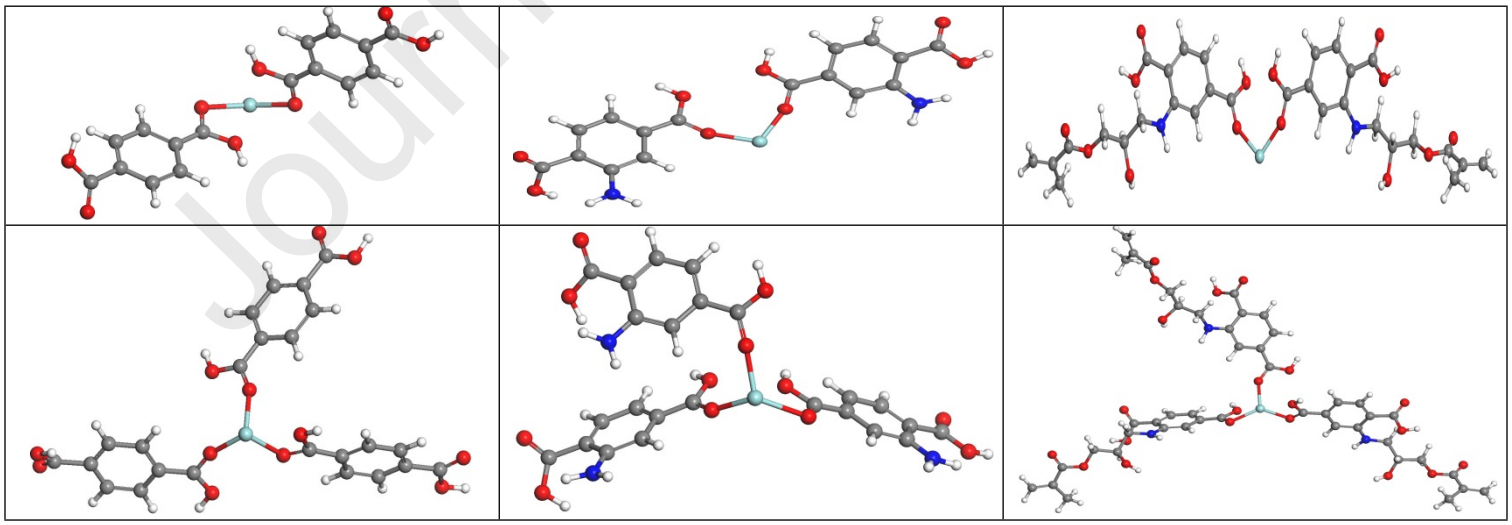

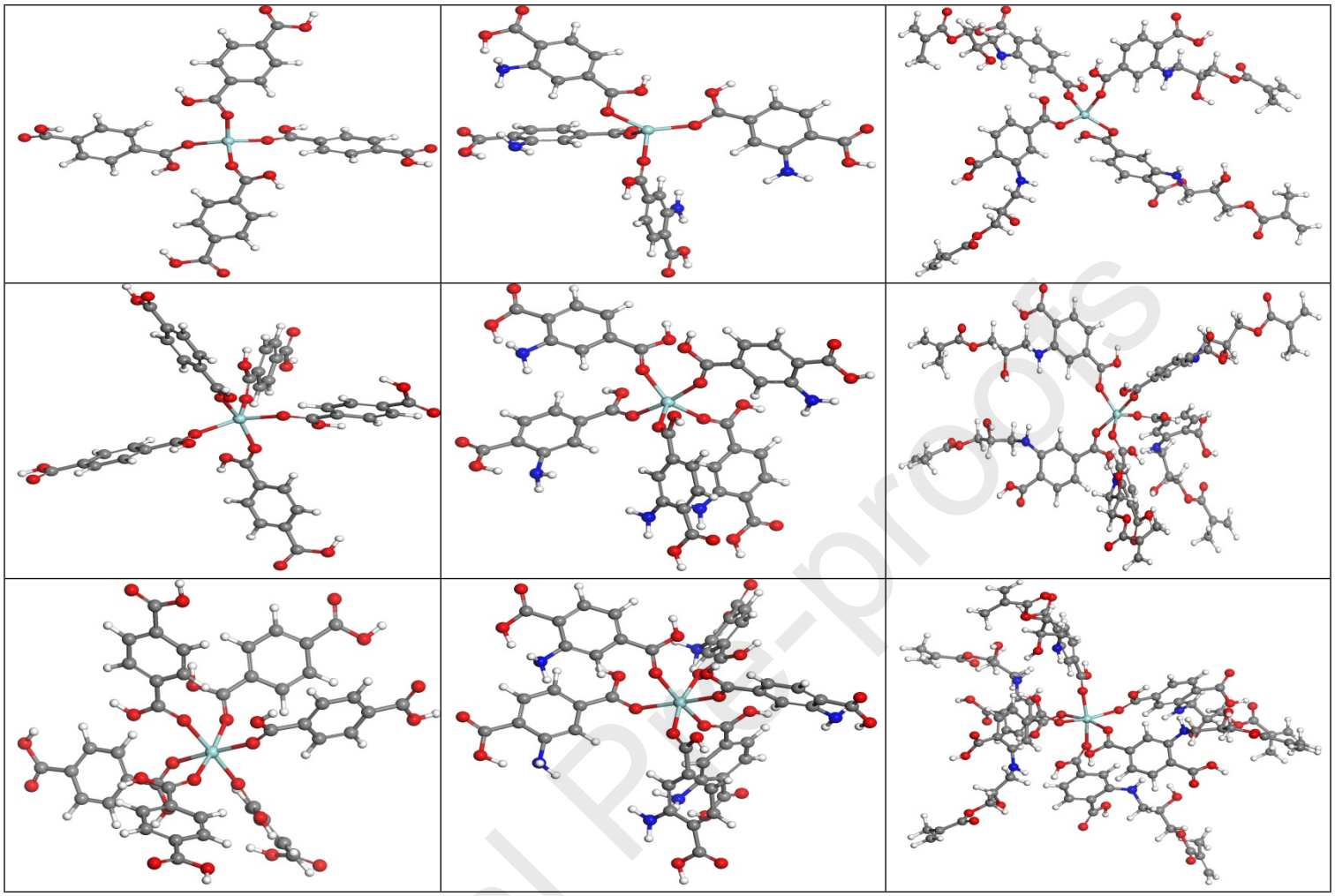

Figure 18. The optimized geometries of zirconium cation (Zr^{+4}) complexes with terephthalic acid (first column), 2-aminoterephtalic acid (second column) and GMA-functionalized 2-aminoterephetalic acid (third column).

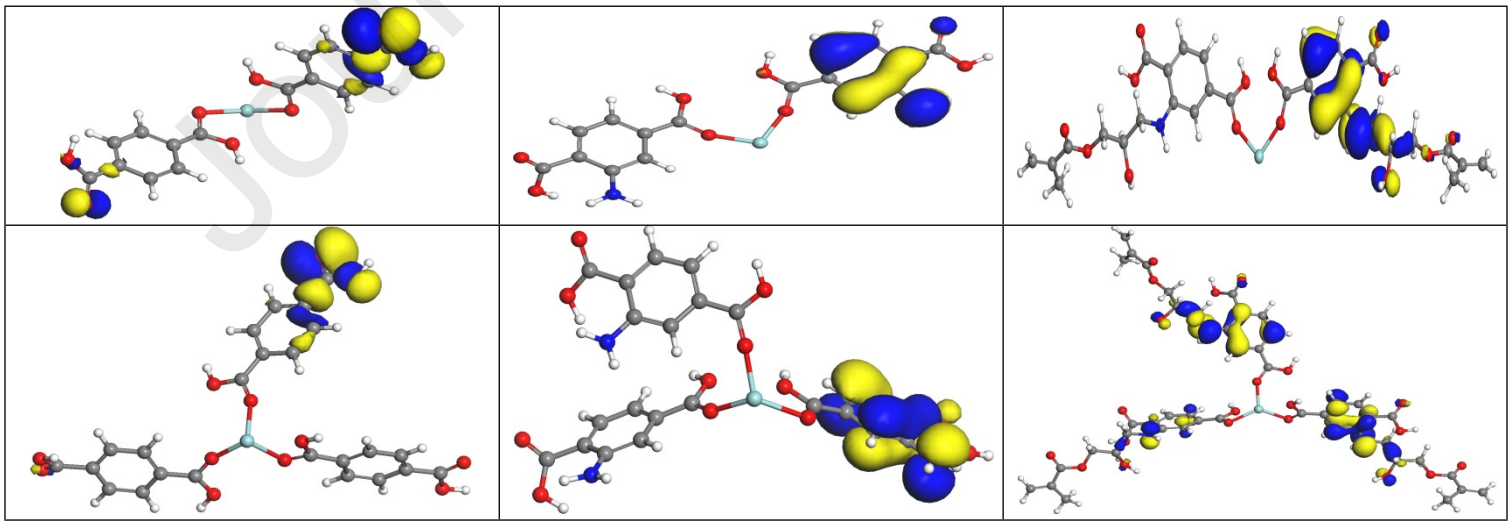

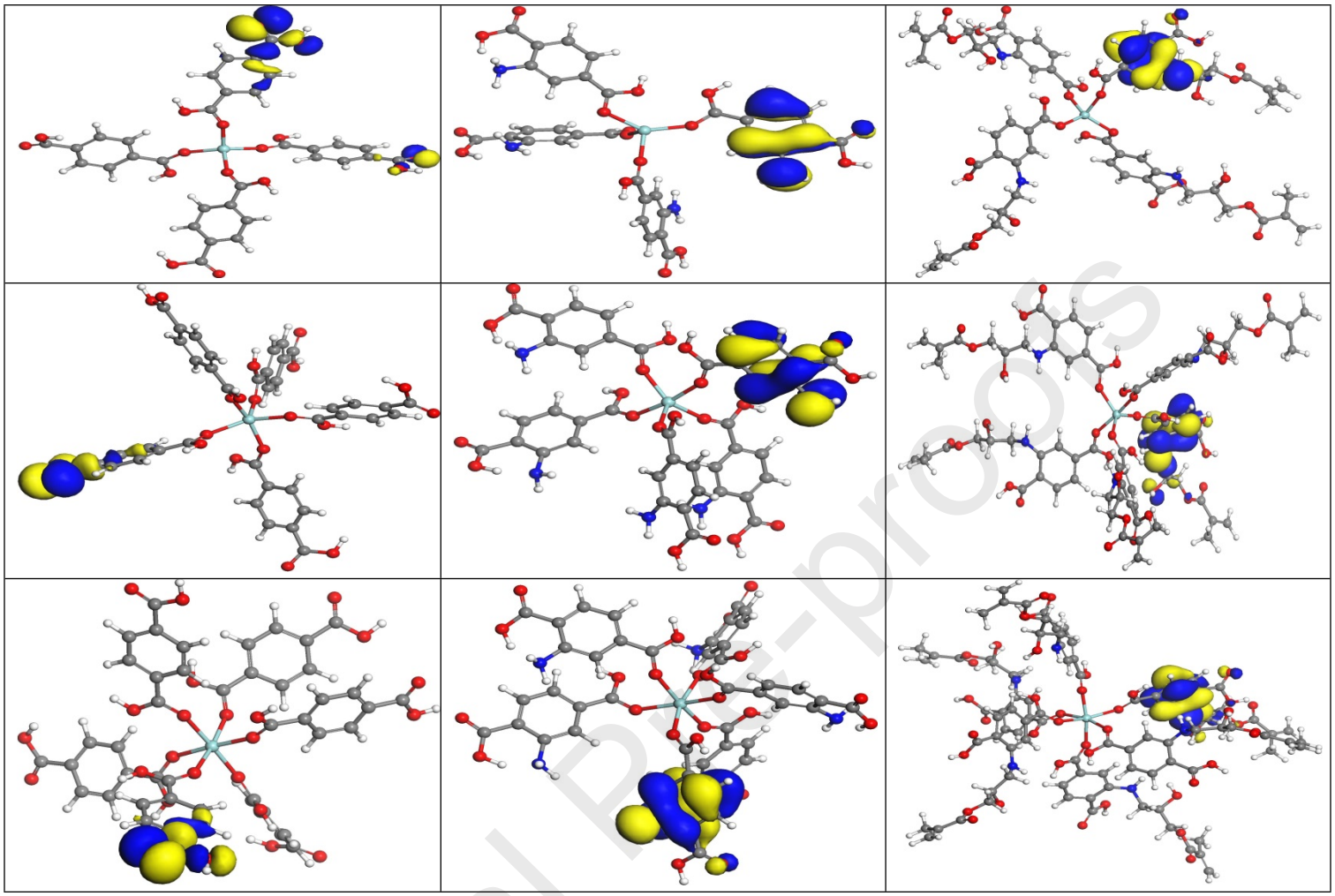

Figure 19. The HOMO of zirconium cation (Zr^{+4}) complexes with terephthalic acid (first column), 2-aminoterephtalic acid (second column) and GMA-functionalized 2-aminoterephetalic acid (third column).

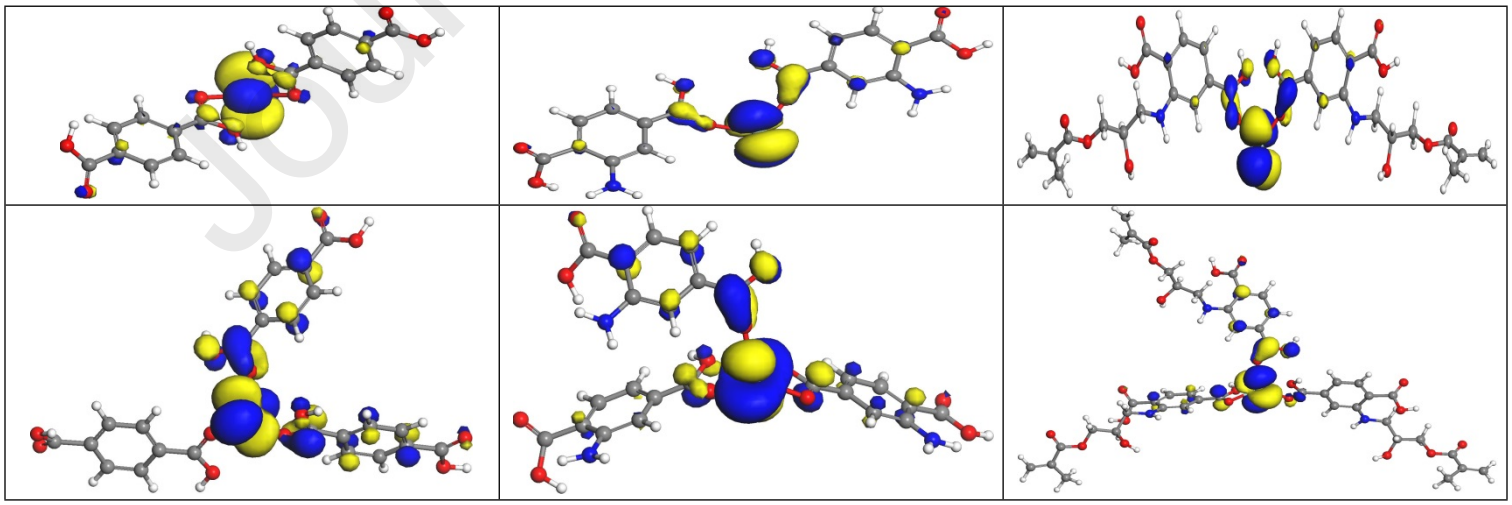

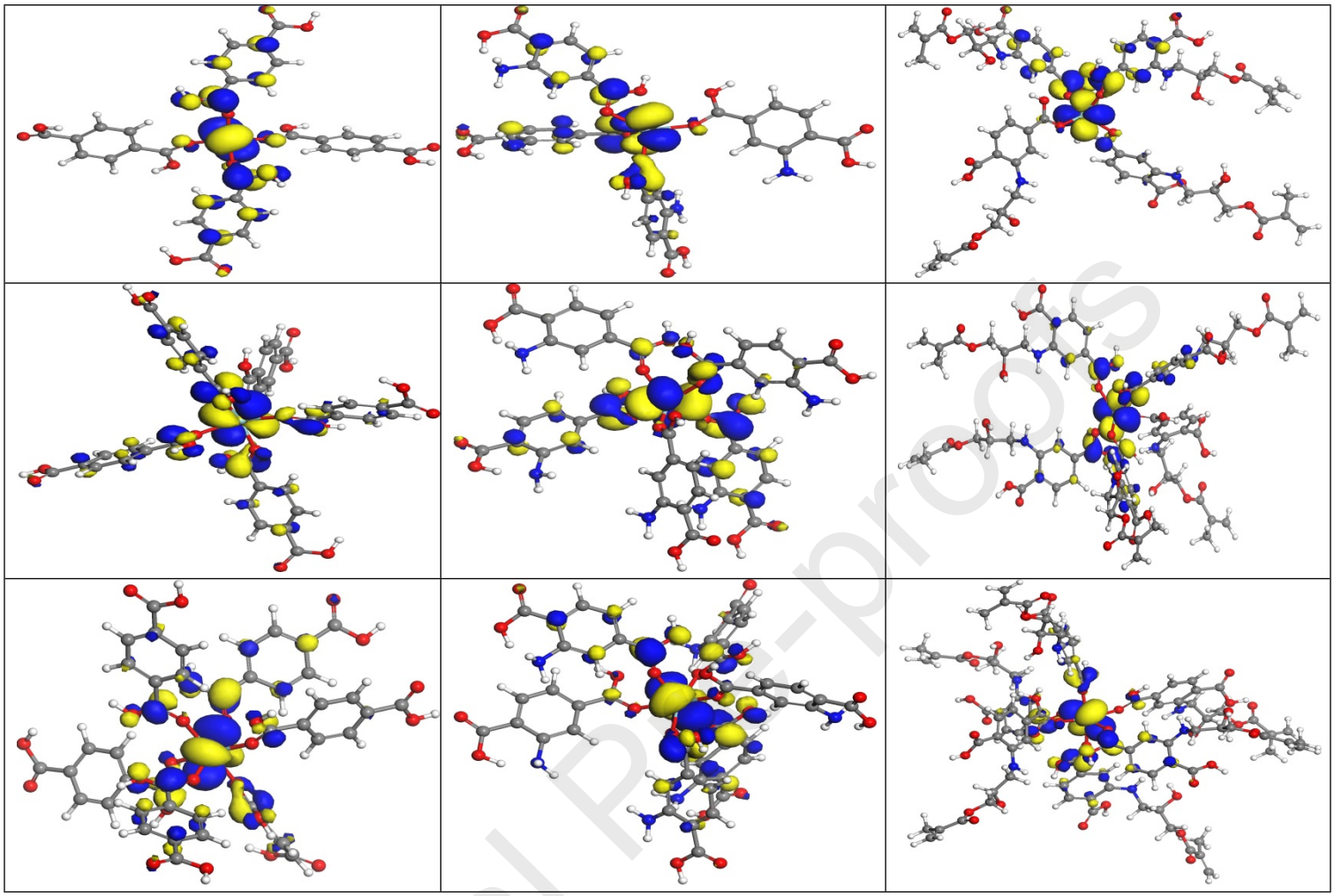

Figure 20. The LUMO of zirconium cation (Zr^{+4}) complexes with terephthalic acid (first column), 2-aminoterephtalic acid (second column) and GMA-functionalized 2-aminoterephetalic acid (third column).

Table 1. Extracted data from the micro-hardness test for the EP, UIO/EP, UIN/EP and GMA-UIN/EP samples after the Vickers micro-hardness test with a load of 0.1 kg at an indentation time of 10 seconds.

Feature↓ Samples→	**EP**	**UIO/EP**	**UIN/EP**	**GMA-UIN/EP**
Vickers hardness (MPa)	0.98	1.96	0.99	1.96
Diagonal lengths (mm)	442.6	284.2	343.1	275.1

Table 2. The amount of the released Zr cations from the UIO-66, UIO-NH_2 and GMA@UIO-NH_2 particles in the 3.5 wt. % chloride solution after 48 h.

Sample	**Time (day)**	**pH**	**Zr (ppm)**	**Organic compounds (ppm)**
UIO-66	2	2	10	40.9
		7.5	4	8
		12	35	117
NH_2-UIO	2	2	26	74.5
		7.5	3	7
		12	137	456
GMA@NH_2-UIO	2	2	25	71.1
		7.5	2	5
		12	98	370

- High-performance coating with promising active inhibition/barrier corrosion retardation features was fabricated.
- The *Zirconium*-based *MOFs were constructed* using terephthalic acid and 2-aminoterephthalic acid.
- The excellent barrier properties of the GMA@NH_2-UIO filled epoxy coating were proved.
- The smart pH-sensitive controlled-release activity of the GMA@NH_2-UIO was proved

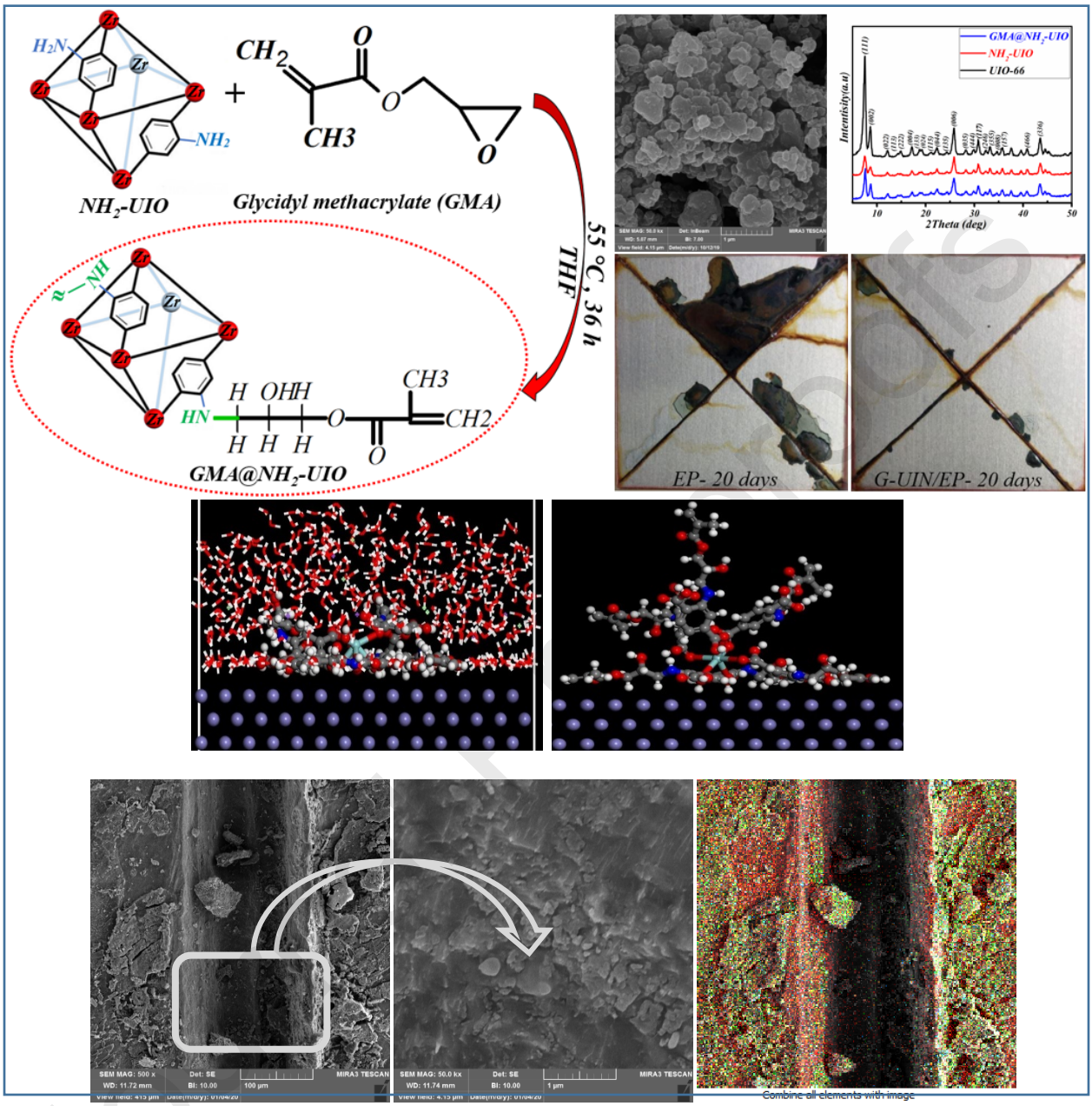

Graphical abstract